Crustal-scale reflection imaging and interpretation by passive seismic interferometry using local earthquakes

Nishitsuji, Yohei; Minato, Shohei; Boullenger, Boris; Gomez, M; Wapenaar, Kees; Draganov, Deyan

DOI
10.1190/INT-2015-0226.1

Publication date
2016

Document Version
Accepted author manuscript

Published in
Interpretation

Citation (APA)
Nishitsuji, Y., Minato, S., Boullenger, B., Gomez, M., Wapenaar, K., & Draganov, D. (2016). Crustal-scale reflection imaging and interpretation by passive seismic interferometry using local earthquakes. *Interpretation*, *4*(3), SJ29-SJ53. https://doi.org/10.1190/INT-2015-0226.1

Full title: Crustal-scale reflection imaging and interpretation by passive seismic interferometry using local earthquakes

April 6, 2016

Abbreviated title: Crustal-scale reflection imaging

Author's names:
Yohei Nishitsuji[1]*, Shohei Minato[1], Boris Boullenger[1],
Martín Gomez[2], Kees Wapenaar[1], Deyan Draganov[1]

Affiliation: [1]Department of Geoscience and Engineering,
Delft University of Technology, Delft, The Netherlands
[2]International Center for Earth Sciences,
Comision Nacional de Energia Atomica, Buenos Aires, Argentina

Corresponding author: Yohei Nishitsuji
address: Department of Geoscience and Engineering,
Delft University of Technology Stevinweg 1, 2628 CN Delft, Netherlands
P.O. Box 5048, 2600 GA Delft, Netherlands
email : y.nishitsuji@tudelft.nl

Abstract

We show application of passive seismic interferometry (SI) using P-wave coda of local earthquakes for the purpose of crustal-scale reflection imaging. We process the reflection gathers retrieved from SI following a standard seismic processing in exploration seismology. We apply SI to the P-wave coda using crosscorrelation, crosscoherence, and multidimensional deconvolution approaches for data recorded in the Malargüe region, Argentina. Comparing the results from the three approaches, we find that multidimensional deconvolution based on the truncated singular-value decomposition scheme gives us a substantially better structural imaging. Although our results provide higher resolution images of the subsurface, it shows less clear images for the Moho in comparison with previous seismic images in the region obtained by receiver function and global-phase seismic interferometry. Above the Moho, though, , we interpret a deep thrust fault and the possible melting zones which are previously indicated by active-seismic and magnetotelluric methods in this region, respectively. The method we propose could be an alternative option not only for crustal-scale imaging, e.g., in enhanced geothermal systems, but also for the lithospheric-scale as well as basin-scale imaging, depending on the availability of local earthquakes and the frequency bandwidth of their P-wave coda.

Introduction

Crustal imaging is vitally relevant for understanding processes like earthquake mechanisms, magmatism, deep geothermal explorations, and basin tectonics. In order to obtain an image of the crust, both active sources (e.g., vibroseis and airguns) and passive sources (e.g., ambient noise and earthquakes) have been used. For the former, the reflection method (e.g., Granath et al., 2010) and refraction method (e.g., Zhao et al., 2013) are well known, whereas for the latter, traveltime tomography (Aki et al., 1977), full waveform tomography (Operto et al., 2006), receiver function (Langston, 1979), and the

Sp-waves method (Doi and Kawakata, 2013) have been applied.

A very attractive passive seismic method is seismic interferometry (SI) (e.g., Aki, 1957; Claerbout, 1968; Campillo and Paul, 2003; Shapiro and Campillo, 2004; Wapenaar, 2004), which retrieves virtual seismic records from existing seismic records. In this study, we focus on body-wave SI. Although the imaging resolution achieved by passive SI might not be easily compatible with the one achieved by the active-source reflection method, it has a potential to contain low-frequency information, i.e., $\leq$ 5 Hz, which enables us to interpret deeper structures, such as in the lower crust and lithosphere. Moreover, as an economically attractive aspect, the shooting cost of the passive seismic method is zero. For reflection retrieval by passive SI, several applications have been already reported, both for ambient noise (e.g., Draganov et al., 2009; Zhan et al., 2010; Ryberg, 2011; Panea et al., 2014; Almagro Vidal et al., 2014) and local earthquakes (e.g., Nakata et al., 2011, 2014).

There are five ways SI can be applied: using correlation (Claerbout, 1968; Duvall et al., 1993); coherence (Aki, 1957); trace deconvolution (Snieder and Şafak, 2006; Vasconcelos and Snieder, 2008a, 2008b); convolution (Slob et al., 2007); and multidimensional deconvolution (MDD; Wapenaar et al., 2008). Nakata et al. (2011) compared the common midpoint (CMP) stacks obtained from SI by crosscorrelation, trace deconvolution, and crosscoherence using traffic noise. The authors suggested that the selection of a proper SI method depends on the data set at hand. In addition to the synthetic comparison of the results obtained from crosscorrelation and MDD by Wapenaar et al. (2011), Nakata et al. (2014) compared SI results obtained using trace deconvolution, crosscoherence, and MDD results (after applying wavefield decomposition), applied to data representing local earthquakes in order to retrieve reflected plane waves. They concluded that MDD provides gathers that have the best signal-to-noise ratio among the compared SI methods.

In this paper, we propose a seismic imaging technique that applies passive SI (two-way traveltime ≤ 20 s) to P-wave coda due to local earthquakes ($2° \leq$ epicentral distances $\leq 6°$). Hereafter, we abbreviate this method as LEPC (local-earthquake P-wave coda) SI. The coda waves are the tail part of a signal consisting of multiply scattered waves (Snieder, 2004). Hence, we assume that their directivity is weak (e.g., Mayeda et al., 2007; Baltay et al., 2010; Abercrombie, 2013), and thus that they illuminate the subsurface beneath the receivers favorably for retrieval of reflections. We apply LEPC SI to data recorded by an exploration-type receiver array called MalARRgue (Ruigrok et al., 2012) that was located in the Malargüe region (Mendoza, Argentina) (Figure 1). Because the west coast of Chile has considerable seismicity due to the Nazca-slab subduction, we choose this region to test LEPC SI.

In the following, we show how to apply LEPC SI using the different retrieval methods (crosscorrelation, crosscoherence, and MDD) for the purpose of crustal-scale reflection imaging.

Study Area and Data

The Malargüe region is located in the northern part of the Neuquén basin, Argentina. This basin has been producing nearly half of the Argentine hydrocarbons, but has also been providing geothermal power. The Peteroa Volcano, which is an active volcano in the Andes Mountains in the Malargüe region, is situated close to part of the array we use (Figure 1). The locations of local earthquakes that occurred in 2012 around the Malargüe region are shown in Figure 1 on a topography map (Becker et al., 2009). The source locations of the earthquakes are provided by Java version of Windows Extracted from Event Data (JWEED) operated by the Incorporated Research Institutions for Seismology (IRIS). We define local earthquakes as those earthquakes whose epicentral distances are between 2° and 6°. This definition is close to the one introduced by Kayal (2008). For the sake of terminological clarification, regional earthquakes, which we do not use in this study, are the earthquakes whose epicentral distances are larger than 6°. In Figure

1, we indicate with triangles the location of the part of the MalARRgue that we use in our study: the T-array, which is an linear receiver array deployed at the surface. The T-array consists of two linear subarrays: the TN-array with 19 stations spaced every 2 km (labeled TN02 to TN20; white triangles in Figure 1), oriented in the NNW direction; the TE-array with 13 stations spaced every 4 km (labeled TE01 to TE13; black triangles in Figure 1), oriented in the ENE direction. These stations are three-component velocity sensors. The 115 circles and 210 stars indicate the location of the local earthquakes recorded by the TN- and TE-array, respectively, and characterized by sufficient signal-to-noise-ratio of the P-wave coda. The TE-array recorded a higher number of earthquakes than the TN-array, because the TE-array was operating longer. The coverage of back azimuth of these earthquakes with respect to the T-array is wide (see Figures 1 and 2). A complete list of the local earthquakes used in this study is shown in Table 1.

Local-Earthquake P-wave Coda Seismic Interferometry (LEPC SI)

Crosscorrelation

In Claerbout (1968), virtual reflection traces were retrieved from the autocorrelation of the recorded transmission response in a horizontally layered medium. Later, he conjectured that in 3D inhomogeneous media, one has to use crosscorrelation to retrieve the reflection response between two receivers at the surface. This was proven by Wapenaar (2004) for an arbitrary inhomogeneous elastic medium. The author showed that the Green's function $G^{v,t}_{p,q}(\mathbf{x}_A, \mathbf{x}_B, \omega)$, representing particle-velocity measurement (v) in the p-direction at a receiver at $\mathbf{x}_A$ due to a point single-force (t) at $\mathbf{x}_B$ in the q-direction, can be retrieved from the crosscorrelation of observed particle-velocity measurements v^{obs}_p and v^{obs}_q at $\mathbf{x}_A$ and $\mathbf{x}_B$, respectively, from uncorrelated noise sources in the subsurface:

$$2Re\{G^{v,t}_{p,q}(\mathbf{x}_A,\mathbf{x}_B,\omega)\}S_N(\omega) \approx -\left\langle \left\{v^{obs}_p(\mathbf{x}_A,\omega)\right\}^* \left\{v^{obs}_q(\mathbf{x}_B,\omega)\right\}\right\rangle. \quad (1)$$

The above equation is written in the frequency domain, indicated by the angular frequency ω; the asterisk denotes complex conjugation; $\langle\rangle$ indicates averaging over source realizations; and the particle-velocity measurements are in the p- and q-directions. The observed data v^{obs} is representing the superposition of recordings from uncorrelated noise sources distributed along a surface that illuminated the received from all directions. $S_N(\omega)$ denotes the power spectrum of the noise. Due to the source-receiver configuration in this study, we exclude the direct wave, which would not fall inside the stationary-phase region for retrieval of reflections. This happens because the epicentral distances of the earthquakes are relatively long compared to their hypocentral depth. We thus aim to use arrivals characterized by slowness smaller than the ones characterizing the direct waves. Note that the exclusion of the direct waves might give rise to artifacts in the retrieved response. Nevertheless, these artifacts should not pose a problem as long as our main aim is to recover the primary reflections. Moreover, having sufficiently long recordings of coda waves would ensure illumination of the receivers from all directions due to equipartitioning. In such a case, one can exchange the noise recordings in equation (1) by recordings of coda waves v^c. For our application, we define an observed P-wave coda of a local earthquake as

$$v^c_z(\mathbf{x}_A,\omega) = G^c_z(\mathbf{x}_A,\mathbf{x}_S,\omega)E(\mathbf{x}_S,\omega), \quad (2)$$

where z indicates that we are using the vertical component of the recordings and $E(\mathbf{x}_S,\omega)$ is the Fourier transform of the source time function (STF) of a local earthquake at $\mathbf{x}_S$ in the subsurface. As P-wave coda, we use the part of the recording after the direct arrival of the P-phase and before the direct arrival of the S-phase.

Because of the limitation on the length of the coda recordings, we cannot expect that the receivers would be illuminated equally well from all directions. Because of this, we would like to repeat the correlation for many local earthquakes with wide distribution of the back azimuth (see Figures 1 and 2) and to average the separate correlations. Thus we rewrite equation (1) as

$$2Re\left\{G_{z,z}^{v,t}(\mathbf{x}_A,\mathbf{x}_B,\omega)\right\}\bar{S}_E(\omega) \propto -\sum_{S=1}^{n}[\{v_z^c(\mathbf{x}_A,\omega)\}^* v_z^c(\mathbf{x}_B,\omega)], \tag{3}$$

where we have exchanged $\langle\rangle$ of equation (1) by a summation over the independent local earthquakes. $\bar{S}_E(\omega)$ denotes the average power spectrum of the STF over the earthquakes.

Crosscoherence

The crosscoherence method (Aki, 1957) is a technique to normalize the amplitude among different source or receiver pairs. By applying SI by crosscoherence instead of crosscorrelation we expect to retrieve better signal-to-noise ratio in terms of the phase in comparison with the crosscorrelation (e.g., Prieto et al., 2009; Nakata et al., 2011). To apply SI by crosscoherence, we rewrite equation (3) as

$$2Re\left\{G_{z,z}^{v,t}(\mathbf{x}_A,\mathbf{x}_B,\omega)\right\} \propto \sum_{S=1}^{n}\frac{\{v_z^c(\mathbf{x}_A,\omega)\}^* v_z^c(\mathbf{x}_B,\omega)}{|v_z^c(\mathbf{x}_A,\omega)||v_z^c(\mathbf{x}_B,\omega)|+\varepsilon}, \tag{4}$$

where ε denotes a stabilization factor (also called a damping factor or a regularization parameter). Since the crosscoherence enhances both the signal and the noise, it is important to have data that is not dominated by noise. Note that in the above equation, the retrieved Green's function is no longer modulated by the average power spectrum of the

STF, as the crosscoherence eliminates it.

Multidimensional Deconvolution (MDD)

While the aforementioned crosscorrelation and crosscoherence calculate the reflection response trace by trace, MDD is a receiver-array-based SI method that calculates the reflection response (the scattered Green's function in Wapenaar et al., 2011) simultaneously for all observed responses via matrix inversion. Although the application of MDD requires regularly-spaced receivers, a point-spread function (PSF), and a regularization approach for the matrix inversion, this technique theoretically removes the influence of the (variation of the) STF of the sources, takes intrinsic attenuation into account (which is not the case for correlation nor coherence) and compensates for possibly inhomogeneous illumination of the receivers by the coda wavefield.

The PSF is a well-known gauge for imaging quality in optics, such as microscopy. In exploration seismology, the PSF is used to quantify the effect of the source and receiver distribution and of the STF on the imaging results. In analogy with this, van der Neut et al. (2010, 2011) showed that the result from SI by crosscorrelation could actually be seen as the blurring (temporal and spatial convolution) of the desired scattered Green's function with a PSF. This PSF is obtained from the crosscorrelation of recordings at the receivers at the surface as if above the receivers there were a homogeneous half space (e.g., Wapenaar et al., 2011). Nakahara and Haney (2015) recently showed that the PSF could also be used for studying earthquake sources. Application of SI by MDD is actually deconvolving the crosscorrelation result by the PSF. To obtain the required wavefield for the retrieval of the correlation result and the PSF, one can apply wavefield decomposition at the Earth's surface (Nakata et al., 2014). This, though, would require a good velocity model for the near surface, which in areas like Malargüe, characterized by strong lateral inhomogeneity, is not readily available. Because it is not possible to obtain measurements as if the Earth's surface were covered by a homogeneous half space, following Wapenaar et al. (2011) we use an approximate relation for the application of SI by MDD:

$$\sum_{S=1}^{n} \left[\left\{ v_z^c(\mathbf{x}_A,\omega) \right\}^* v_z^c(\mathbf{x}_B,\omega) \right] - 2\Gamma(\mathbf{x}_B,\mathbf{x}_A,\omega) \propto \iint_{\partial D_0} G_{z,z}^{scatt,d}(\mathbf{x}_B,\mathbf{x},\omega)\Gamma(\mathbf{x},\mathbf{x}_A,\omega)d^2\mathbf{x} \tag{5}$$

where Γ is the approximated PSF and $G_{z,z}^{scatt,d}$ is the scattered Green's function due to a dipole source. Figure 3 shows a schematic image of the terms in equation (5). The integral in equation (5) is taken along the receiver positions (Earth's surface ∂D_0). A derivation of equation (5) is given in Appendix A. Just like Wapenaar et al. (2011), we look at the recorded wavefield as a part that will be recorded at the receivers in the absence of a free surface and a part due to the presence of the free surface (which is the former after being reflected at the free surface at least once). The Γ in equation (5) (see Figures 9c and 9f later in this paper) can be estimated by extracting time-windowed signals from the crosscorrelation at $\mathbf{x}_A$ and $\mathbf{x}_B$ (the right-hand side of equation 3) (see Figures 9c and 9f later in this paper) of the wavefield that would be recorded in the absence of a free surface at the receivers. The signals that make up Γ exhibit a butterfly-shaped window around $t = 0$ (see Figures 9c and 9f later in this paper), narrowest when $\mathbf{x}_A = \mathbf{x}_B$. We assume that the contribution from the crosscorrelation at $\mathbf{x}_A$ and $\mathbf{x}_B$ of the wavefield that would be recorded due to the presence of a free surface at the receivers is sufficiently small to be neglected (van der Neut et al., 2010; Wapenaar et al., 2011). Note that the numerical test showed that the approximation can provide the correct scattered Green's function with small inversion artifacts (van der Neut et al., 2010). For notational simplicity, we define the left hand-side of equation (5) as

$$C'(\mathbf{x}_B, \mathbf{x}_A, \omega) = \sum_{S=1}^{n} \left[\left\{ v_z^c(\mathbf{x}_A, \omega) \right\}^* v_z^c(\mathbf{x}_B, \omega) \right] - 2\Gamma(\mathbf{x}_B, \mathbf{x}_A, \omega). \tag{6}$$

Substituting equation (6) in equation (5), we obtain

$$C'(\mathbf{x}_B, \mathbf{x}_A, \omega) \propto \iint_{\partial D_0} G_{z,z}^{scatt,d}(\mathbf{x}_B, \mathbf{x}, \omega) \Gamma(\mathbf{x}, \mathbf{x}_A, \omega) d^2\mathbf{x}. \tag{7}$$

Equation (7) can be discretized by fixing the position of $\mathbf{x}_B$ and varying the receiver position $\mathbf{x}_A$:

$$\begin{pmatrix} C'(\mathbf{x}_B, \mathbf{x}_1, \omega) \\ C'(\mathbf{x}_B, \mathbf{x}_2, \omega) \\ \vdots \\ C'(\mathbf{x}_B, \mathbf{x}_m, \omega) \end{pmatrix} \propto \begin{pmatrix} \Gamma(\mathbf{x}_1, \mathbf{x}_1, \omega) & \Gamma(\mathbf{x}_2, \mathbf{x}_1, \omega) & \cdots & \Gamma(\mathbf{x}_m, \mathbf{x}_1, \omega) \\ \Gamma(\mathbf{x}_1, \mathbf{x}_2, \omega) & \Gamma(\mathbf{x}_2, \mathbf{x}_2, \omega) & \cdots & \Gamma(\mathbf{x}_m, \mathbf{x}_2, \omega) \\ \vdots & \vdots & \ddots & \vdots \\ \Gamma(\mathbf{x}_1, \mathbf{x}_m, \omega) & \Gamma(\mathbf{x}_2, \mathbf{x}_m, \omega) & \cdots & \Gamma(\mathbf{x}_m, \mathbf{x}_m, \omega) \end{pmatrix} \begin{pmatrix} G_{z,z}^{scatt,d}(\mathbf{x}_B, \mathbf{x}_1, \omega) \\ G_{z,z}^{scatt,d}(\mathbf{x}_B, \mathbf{x}_2, \omega) \\ \vdots \\ G_{z,z}^{scatt,d}(\mathbf{x}_B, \mathbf{x}_m, \omega) \end{pmatrix}, \tag{8}$$

where we assume that we have m receivers in total. We can simplify equation (8) using matrix-vector notation:

$$\mathbf{c}' \propto \mathbf{\Gamma}\mathbf{g}, \tag{9}$$

where $\mathbf{\Gamma}$ is a $m \times m$ matrix, respective $\mathbf{c}'$ and $\mathbf{g}$ are $m \times 1$ column vectors showing receiver gathers. Constructing multiple column vectors using equation (8) for variable $\mathbf{x}_B$ and arranging them as columns of a matrix, we obtain:

$$\mathbf{C}' \propto \mathbf{\Gamma}\mathbf{G}, \tag{10}$$

where $\mathbf{C}'$ and $\mathbf{G}$ are $m \times m$ monochromatic matrices containing $C'(\mathbf{x}_m, \mathbf{x}_m, \omega)$ and $G_{z,z}^{scatt,d}(\mathbf{x}_m, \mathbf{x}_m, \omega)$, respectively. Estimating the dipole scattered Green's function in equation (10) requires matrix inversion:

$$\mathbf{G}' \propto [\mathbf{\Gamma}]^{-g}\,\mathbf{C}', \tag{11}$$

where $[\mathbf{\Gamma}]^{-g}$ is a generalized inverse of $\mathbf{\Gamma}$, and $\mathbf{G}'$ is an estimate of $\mathbf{G}$.

Note that our receiver configuration might not be optimal for MDD studies. The number of receivers we have is relatively small - 19 and 13 for the TN- and TE-array, respectively. Fewer receivers leads to more severely ill-posed solutions in the inversion process. Two approaches to stabilize the MDD in equation (11) have been used: a damped least-squares (Menke, 1989); and a singular-value decomposition (SVD; Klema and Laub, 1980).

MDD by Damped Least Squares

The damped least-square solution is a commonly used approach for MDD studies (e.g., Wapenaar et al., 2008; van der Neut et al., 2011; Boullenger et al., 2015). This scheme can be directly adapted to the generalized inverse matrix in equation (11), resulting in

$$\mathbf{G}' \approx \left[\mathbf{\Gamma}^{\dagger}\mathbf{\Gamma} + \varepsilon\mathbf{I}\right]^{-1}\mathbf{\Gamma}^{\dagger}\mathbf{C}', \tag{12}$$

where ε and $\mathbf{I}$ indicate a stabilization factor and the identity matrix, respectively. The symbol † denotes the complex conjugate transpose matrix. In practice, $\mathbf{\Gamma}$ is estimated in the time domain and then transformed to the frequency domain by the Fourier transform. A disadvantage of this scheme is that choosing an appropriate stabilization factor tends to be inevitably subjective because it is difficult to evaluate the data redundancy in a quantitave way.

MDD by Truncated Singular-Value Decomposition (SVD)

There are only a few examples of MDD based on the truncated SVD scheme (e.g., Minato et al., 2011, 2013). The concept of the truncated SVD scheme is fundamentally close to the principal component analysis (Pearson, 1901) in machine learning, which is also called a subspace method or Karhunen-Loève expansion, and the latent semantic analysis (Borko and Bernick, 1963) in natural language processing. For example, both the truncated SVD scheme and the principal component analysis find the data directions (axes) from the eigenvectors of the covariance matrix using the SVD algorithm via Lagrange multiplier. Here, we briefly introduce the truncated SVD scheme.

Let us define the SVD of $\mathbf{\Gamma}$ in equation (10) as:

$$\mathbf{\Gamma} = \mathbf{U} \begin{pmatrix} \mathbf{\Delta}_r & \mathbf{0} \\ \mathbf{0} & \mathbf{0} \end{pmatrix} \mathbf{V}^\dagger, \tag{13}$$

where $\mathbf{U}$ is a a left-singular matrix (orthonormal-basis matrix), $\mathbf{V}$ is a right-singular matrix (orthonormal-basis matrix). $\mathbf{V}^\dagger$ is the adjugate (adjoint) matrix that is the complex conjugate transpose matrix of $\mathbf{V}$. $\mathbf{\Delta}_r$ is an $r \times r$ diagonal matrix whose elements are the singular values of the monochromatic matrix $\mathbf{\Gamma}$, obtained by truncation. We define the dimension r as the number of significant singular values by specifying a threshold value. Then, we adapt the Moore-Penrose pseudoinverse (Golub and van Loan, 1983) for equation (13):

$$[\mathbf{\Gamma}]^{-g} = \mathbf{V} \begin{pmatrix} \mathbf{\Delta}_r^{-1} & \mathbf{0} \\ \mathbf{0} & \mathbf{0} \end{pmatrix} \mathbf{U}^{\dagger}, \tag{14}$$

where $\mathbf{U}^{\dagger}$ is the adjugate (adjoint) matrix of $\mathbf{U}$. In the following section, we show the MDD results of the damped least-squares scheme and the truncated SVD scheme.

Data Processing

Preprocessing

Our first step in the preprocessing is to remove the instrument response from the recorded data. After that, we compute power spectral densities (PSD) of the local earthquakes to determine a frequency band that exhibits adequate signal-to-noise ratio. Examples of PSD of the local earthquake for the TE-array are shown in Figure 4. Analyzing the PSDs, we choose the frequency band 1-5 Hz for further seismic processing. We set the high end of the band at 5 Hz due to the presence of irregular noise around 8 Hz (see Figure 4), which is masking the signals from weaker earthquakes. The nature of this noise is not clear. The stations are away from continuous anthropogenic sources, so this could be excluded as main contributor. Since this noise is almost continuously seen over the records in MalARRgue, it might be connected to the wave action in the nearby lake Llancanelo (Figure 1), but possibly also with deeper activity below the volcanic cones in the vicinity of the array. The noise, which is also continuously seen around 0.3 Hz, likewise to be due to the double-frequency microseisms. In principle, one can use higher frequency (if available) for LEPC SI to obtain images of shallower structures, e.g., at basin scale. For speeding up the computations, after the band-pass filtering, we downsample the data to 0.05 s (Nyquist frequency of 10 Hz) from the original sampling of 0.01 s (Nyquist frequency of 50 Hz).

The useful window length of the coda of the *P*-wave phase is explained in Figure 5 as a function of the epicentral distance. To calculate the times in Figure 5, we use the regional velocity model of Farías et al. (2010) down to 110 km and ak135 (Kennett et al., 1995) deeper than that. In order to only extract the P-wave coda without the direct wave that usually brings strong directivity in the SI results, we refer to the scaling relation between the moment magnitude, M_{W}, and the source duration of the earthquakes (Kanamori and Brodsky, 2004) assuming that M_{W} is proportional to M_{b} for our magnitude range (Atkinson and Boore, 1987). Thus, our coda-waves extraction window starts at the time obtained from the summation of the time of the expected *P*-phase arrival and the expected time length of the STF.

For the local earthquakes ($2° \leq$ epicentral distances $\leq 6°$), surface waves are expected to arrive almost simultaneously with the *S*-wave phase onset or later (Kennett et al., 1995). To make sure that the coda does not contain surface waves related to the earthquake, our coda-wave extraction window terminates a few seconds before the observed *S*-wave phase onset.

With the above window-length selection criteria, the coda duration is shorter for some earthquakes, but still we have sufficient coda duration (e.g., 15-70 s) for the subsurface imaging. An example of the coda extraction is shown in Figure 6. For subsequent seismic processing, we use only the P-wave coda (the blue window) extracted from the vertical component. It is difficult to estimate how much converted *S*-wave phases are present within the P-wave coda, but they most probably are present. Especially, SV-waves are expected to be present on the vertical component we use. In this study, we assume that the SV-waves are not dominantly recorded for deeper earthquakes (e.g., 50-100 km) due to their small slowness. For shallower earthquakes (e.g., 0-50 km), the SV-waves can be recorded with spatial aliasing due to the larger ray parameter compared to the ray parameter for P-waves. However, the crosscorrelation and summation process should suppress such aliasing effects, emphasizing the reflection responses of the structures.

Note that the transverse component in Figure 6 is displayed only for the purpose of data comparison with the vertical component.

After extracting the P-wave coda from each selected local earthquake, we interpolate missing traces at certain stations (e.g., due to technical problems in the acquisition) using their two closest neighboring station records using linear interpolation. For example, if TE10 has a missing trace, we interpolate it only when TE09 and TE11 have non-missing traces for that time. In Figure 7, we show the number of interpolated traces (what we also call events).

LEPC SI Applications

Crosscorrelation and Crosscoherence Processing

We apply crosscorrelation to the preprocessed data of the T-array from MalARRgue after applying amplitude normalization per coda-wave window per station. The normalization is used to bring per station the correlation results from each local earthquake to a comparable amplitude and thus to let each correlation have the same weight in the summation over the earthquakes. We test utilization of energy normalization, normalization by the maximum amplitude, and normalization by the maximum amplitude followed by spectral whitening. In Figures 8b-d, we show the three respective results obtained from autocorrelation, which represent retrieved zero-offset traces. In Figure 8a, we show the retrieved zero-offset trace obtained without any normalization. As can be seen from Figures 8a-c, there is no significant difference between the results with and without normalizations, implying that for the earthquakes we choose, the recordings from the different earthquakes have comparable amplitudes in the 1-5 Hz frequency band. Nevertheless, we can notice small differences among the results, so it is better to use normalization before correlation given its numerical robustness. In Figure 8e, we show the retrieved zero-offset trace obtained from autocoherence. In Figure 8d, we show for completeness of comparison another correlation result obtained after energy normalization and spectral whitening. The whitening was performed using a running window of 0.025 Hz width. Note that energy normalization followed by spectral whitening makes the result retrieved by correlation (Figure 8d) close to the one retrieved by coherence (Figure 8e). This is because normalization and spectral whitening mathematically approximates coherence. In this study, we use crosscorrelation and crosscoherence. For retrieval using crosscorrelation, we choose to use preprocessing by energy normalization without spectral whitening (as in Figure 8b), so that we could see clear differences between the results from crosscorrelation and those from crosscoherence.

Figures 9a and 9d show retrieved common-source gathers (at positive and negative times) obtained using crosscorrelation for a virtual source at TN11 (the middle station in the TN-array) and TE07 (the middle station in the TE-array), respectively. It can be seen that the common-source gathers exhibit asymmetrically retrieved events with respect to two-way traveltime 0 s, indicating that the coda we use is not illuminating the stations equally from all directions. Even though Mayeda et al. (2007), Baltay et al. (2010), and Abercrombie (2013) assumed apparent weak to no directivity of the coda, i.e., isotropic energy flux, due to the expected averaging out of radiation pattern of the earthquake, Paul et al. (2005) and Emoto et al. (2015) found that the energy flux of the coda is not isotropic. In the case that the coda has no directivity, the causal and acausal parts of the common-source gathers obtained from crosscorrelation would result in a purely symmetric gather. When the coda has directivity, the common-source gather would exhibit asymmetry as shown in Figure 9d.

A possible explanation of the directivity in the coda, which is most likely the case with our data as well, is that it is associated with the direct-wave passages (e.g., Emoto et al., 2015). Emoto et al. (2015) discussed that the coda consists of forward scattered waves (early coda), which have directivity, and multiply scattered waves (later coda), which have no directivity.

For the results retrieved from SI by crosscorrelation and crosscoherence, we correct for the asymmetric results (Figures 9a and 9d) by combining part of the positive and parts of the negative times as follows. To obtain a final retrieved common-source gather, we use the acausal part of the retrieved result for traces to the west of the virtual-source position, reverse this part in time, and concatenate it to the causal part of the retrieved result for traces to the east of the virtual-source position (Figures 9b and 9e). This processing is strictly valid for horizontally layered medium. In our case, since we rely on secondary scattering, we can still use this processing provided that the scattering results in the illumination of the array mainly from the west of the array and that the structures below the array are not complex.

For the next processing step, we apply a deterministic spiking deconvolution to remove the STF of the retrieved virtual source from each of the retrieved common-source gathers. The deterministic spiking deconvolution is a technique that compress the STF (e.g., known from observation) using the least-squares method. The STF are estimated from the retrieved zero-offset traces at each virtual-source position by extracting a time-window around time 0 s (Figure 10). Following the conventional seismic processing, we mute the first breaks and all the events above them from the common-source gathers for the both TN- and TE-array as shown in Figure 11. Our estimates of the first breaks are about 3400 m/s (a constant velocity) for both arrays. After that, we re-sort the traces into CMP gathers and apply normal moveout velocity analysis to the data using semblances. In Figure 12, two examples of velocity semblance are shown with the regional velocity model by Farías et al. (2010) indicated by the dashed magenta lines. There is a good correspondence between the regional model and peaks in the middle part of the semblance. For example, the bright spots in the semblance around 10-11 s (the left panels in Figure 12) correspond to the range of the possible Moho velocity in Farías et al. (2010). In this study, though, we use for normal-moveout correction and migration the regional velocity model from Farías et al. (2010) because this simplifies the interpretation during the comparison of the current result with our previous result from application of global-phase SI

(Nishitsuji et al., 2016). The global-phase SI is an autocorrelation SI that uses global phases (e.g., *PKiKP*).

After obtaining stacked sections along both arrays we apply predictive deconvolution to suppress possible multiples from the top basement using the estimated depth of the top of basement beneath MalARRgue (Nishitsuji et al., 2014). Finally, we apply Kirchhoff post-stack time migration (KTM; Yilmaz, 1987) to move dipping structures to their true location in the model. As a final processing step, we apply lateral regularization in the horizontal direction to obtain better imaging in terms of structural interpretation. For the lateral regularization, we use smoothed discretized splines determined by the generalized cross-validation (Garcia, 2010). The stacked sections before and after the mentioned processing (predictive deconvolution, KTM, and lateral regularization) for the TN- and TE-array are shown in Figures 13a,b and 14a,b, respectively.

The seismic processing of the results retrieved from SI by crosscoherence is the same as for the results retrieved by crosscorrelation, except for the step of applying spiking deconvolution of the STF, which is not needed. The processed stacked section obtained from SI by crosscoherence are displayed in Figures 13c and 14c. For Figures 13c and 14c, we select the results obtained using a stabilization factor of 1 % of the maximum in the amplitude spectrum. In our case, we did not see significant differences when using stabilization factors between 1 % and 5 %.

MDD Processing

The data processing for application of SI by MDD differs only in a few steps from the other two LEPC (crosscorrelation and crosscoherence), interferometric applications. Due to the fact that MDD intrinsically deconvolves for the STF of the earthquake sources and compensates for directivity in the illumination, neither spiking deconvolution for the STF of the retrieved virtual source nor selective utilization of parts of the causal and acausal times are needed. Instead, it is necessary to obtain the estimated PSF for solving the inverse problem of the approximated MDD in equation (11). In Figures 9c and 9f, we show two examples of PSFs extracted (cut away with tapered edges) from the retrieved crosscorrelation results in Figures 9a and 9d, respectively. We extracted the PSF with a butterfly-shaped window around $t = 0$ and narrowest for $\mathbf{x}_A = \mathbf{x}_B$. It aims to include events obtained from the crosscorrelation between waves that are recorded at the surface as direct waves from secondary sources in the subsurface (the scatterers and reflectors). Note that the approximated PSFs are shown after amplitude normalization among the stations for the purpose of displaying only; we do not use amplitude normalization for the actual MDD processing. The time window for the PSF is based on the velocity used for the first-break muting in Figure 12.

We apply SI by MDD to the LEPC data using the truncated SVD approach to stabilize the inversion. We process the two lines separately - we retrieve virtual-source response along the TN-array using the events recorded by and interpolated along the TN-array; we retrieve virtual-source response along the TE-array using the events recorded by and interpolated along the TE-array. As can be seen from Figure 7, the number of earthquakes for each station per subarray is different. For example, for the TE-array, the number of interpolated events per station is between 200 and 210. This means that several PSFs for the TE-array contain zeros for the matrix inversion. However, we expect that the illumination compensation for the TE-array from the used 210 events will be affected only to a small degree by the zeros in the PSFs due to the random distribution of the zeros. The same can be said for the TN-array as well, but in its case the number of interpolated events per station is around 115 (except for TN02). After the SVD, we truncate singular values with amplitudes with a threshold value of 10 % of the maximum singular value. The singular values under the threshold are considered negligible to retrieve reflection-data estimates. Figure B1 is available in Appendix B that shows the singular values we truncate. The discarded singular values would largely contribute to the ill-posedness of equation (11). In Figures 15a and 15b we show the obtained MDD results in the f-x domain for virtual shots at TN11 and TE07, respectively. We also test application of SI by MDD using the damped least-squares stabilization with a constant stabilization factor for all frequencies, but the results are not as well stabilized as the ones using the truncated SVD scheme (Figure 15).

Results and Interpretation

In Figures 16 and 17, we show the LEPC SI results for the TN- and TE-array, respectively, obtained by MDD using the truncated SVD; we compare these results to the results obtained by global-phase SI by Nishitsuji et al. (2016) who used frequency band 0.3-1 Hz. We design the processing parameters for the basement predictive deconvolution based on the estimated two-way traveltime of the basement multiples (Nishitsuji et al., 2014). For comparison purposes, we use the same processing parameters of KTM for both of the LEPC SI and the global-phase SI results. The reflection imaging exhibits more details than the results from the global-phase SI. The bifurcated Moho and the magma chamber indicated in Figures 16 and 17 are after Gilbert et al. (2006). The gray shades in Figures 16 and 17 indicate the offset where the CMP fold numbers are less than or equal to 5; we do not interpret the results inside the gray shaded areas as we deem this fold insufficient for imaging. The yellow dashed lines are our structural interpretation where the amplitude and phase discontinuities are seen based on the global-phase SI results. We superimpose those interpreted features over the LEPC SI results because it is difficult to tell which features are the artifacts or not in a decisive way. Although one might like to interpret more structures on the LEPC SI results, we only focus on the major features interpreted by the global-phase SI results. Because we would like to keep the correspondence, no horizon interpretations are given for structures shallower than about 7-seconds two-way traveltime, where the global-phase SI results become unclear (Figures 16b and 17b). The global-phase SI results (Figures 16b and 17b) show the limitation in interpreting shallow structures because the subtraction of the average STF for 10 s unavoidably removes some shallow structures. Note that because LEPC SI has retrieved reflections that resulted in imaging structures below the array, we can conclude that there has been sufficient local scattering below the array. This is also expected from the presence of a line of volcanic cones at the surface crossing the TE-array. Local secondary scattering from structures below the array would result in arrivals characterized by small emergence angles at the array; such arrivals will be turned by SI into reflections. As the local earthquakes we use are distanced from the TN- and TE-arrays and the coda window length is limited, if there were little or no local scattering below the array, LEPC SI would not have retrieved reflections.

Since all of the LEPC SI results (crosscorrelation, crosscoherence, and MDD) appear in general to be similar (see Figures 13b-d and 14b-d), one might prefer to use for the interpretation of the other LEPC SI results instead the MDD results. However, if we have a limited number of local earthquakes whose back-azimuth coverage is insufficient with respect to the receiver-array, MDD should in theory work better than the other two methods (Nakata et al., 2014). This is, because for crosscorrelation and crosscoherence to work, a large number of local earthquakes with sufficiently wide back-azimuth coverage is essential for the effective suppression of the cross-talk (e.g., Snieder, 2004; Snieder et al., 2006). On the other hand, assuming a sufficiently good coverage of the local earthquakes is available but the receiver-array is patchy or irregular, both the crosscorrelation and crosscoherence would work, whereas MDD would be ill-posed because it requires regularly-spaced receivers. As shown in Figures 1 and 2, we have good coverage of the local earthquakes recorded at the exploration-type array. This could be the reason why the LEPC SI results in Figures 13b-d and 14b-d show similar results at our scale of interest. Nevertheless, we decide to select the LEPC SI results based on the MDD by truncated SVD scheme in Figures 16 and 17 rather than the others because we find that a few structural features showing more continuity in space. For instance, a horizontal coherent feature around 8 s in Figure 16 and up-dipping (from west to east direction) structures between 13-15 s in Figure 17 are clearer than the images from the other two methods in Figures 13 and 14. More importantly, the PSFs in Figure 15 are smeared in space and time, which means that the crosscorrelation results in Figures 13 and 14 are biased due to the spatial-temporal blurring effect of the PSF. This is also the reason we select the MDD results in Figures 16 and 17.

Interpreting results from the magnetotelluric method, Burd et al. (2014) (the blue dashed line in Figure 1) recently suggested the presence of a possible shallow asthenospheric plume (e.g., 0-100 km in depth) nearby the Peteroa volcano. The authors interpreted this shallow plume as possibly connected to the main upwelling plume whose origin would be around the mantle transition zone (410-660 km in depth). Gilbert et al. (2006) showed the receiver-function imaging at roughly 50 km south of MalARRgue, interpreting a possible bifurcation of the Moho with magma chamber in between (Figure 5 in Gilbert et al., 2006). The study by Nishitsuji et al. (2016) using the global-phase SI confirmed such Moho bifurcation beneath the array of the MalARRgue. Summing up the above interpretations, one could expect a dynamic tectonic regime rather than a static one in this Andean region.

As we described earlier, the reflection imaging of the LEPC SI results exhibits more details than the results from the global-phase SI. As shown by Abe et al. (2007) and Nishitsuji et al. (2016), the vertical imaging resolution in results retrieved by SI would be at least as high as, but potentially higher, than the ones obtained by the receiver-function method. The difference of the resolution in Figures 16 and 17 is largely due to the difference in the used frequency band. Nishitsuji et al. (2016) used global-phase earthquakes with frequency band 0.3-1 Hz, whereas here we use 1-5 Hz for the LEPC SI results. In addition to the correspondence (or similarity) of the structural features (the yellow dashed lines in Figures 16 and 17) between these two different methods, there is another striking feature - a possible major fault in Figure 17a, indicated by the green dashed line, where horizon displacements can be seen. According to the active-seismic reflection profile (the green solid line in Figure 1) and nearby exploration well (LPis x-1) given in Kraemer et al. (2011), deep basement thrust faults, which are reverse faults (see Figure 8a in Kraemer et al., 2011), are expected to exist in this region as a typical feature of foredeep basins (DeCelles and Giles, 1996). Such thrust faults can also be seen in Gimbiagi et al. (2009) and Giambiagi et al. (2012) in their Figures 7b-c and 2 (e.g., cross-section H), respectively. Because the reverse faults beneath LPis x-1 are thought to be dipping to the west, identifying such faults below the TE-array (Figure 17a), but not below the TN-array (Figure 16a) is logical. Thus, we interpret the feature indicated by the green dashed line in Figure 17a as possibly corresponding to one of those deep thrusts.

The blue ellipses in Figure 17 indicate zones where dimmed-amplitude portions can be seen in both the LEPC SI (Figure 17a) and global-phase SI results (Figure 17b). Since both independent methods use acoustic SI approaches, such dimming features might indicate weaker reflection responses in comparison with the other zones. Referring to the previous studies in this region, such weaker reflectivity might be due to the presence of the shallow asthenospheric plume that has been interpreted by Burd et al. (2014). Otherwise, such dimmed amplitudes might be indicative of partial-melting spots that are only locally present.

We also observe that the Moho in the LEPC SI results are not as visually dominant as the ones from the global-phase SI (Nishitsuji et al., 2016) and receiver-function method (Gilbert et al., 2006). This feature could be also found in other high-resolution reflection images by active-seismic sources. For instance, although the reflection results in Singh et al. (2006) and Calvert and McGeary (2013) provided very fine scale of the images (e.g., 50 m in depth after Singh et al., 2006), we find that the Moho in their results is somewhat less prominent than in the image from seismic tomography (e.g., Calvert et al., 2011) and the receiver-function method (e.g., Gilbert et al., 2006). This is probably because the Moho discontinuity is rather better sensed with low frequencies (e.g., ≤ 1 Hz). The active-source reflection in Singh et al. (2006) and LEPC SI in this study used 10-30 Hz and 1-5 Hz, respectively. The seismic tomography in Calvert et al. (2011) and the global-phase SI in Nishitsuji et al. (2016) used 0.03-0.3 Hz and 0.3-1 Hz, respectively.

Therefore, as long as one's goal is the identification of the Moho, using the lower frequencies would in general be sufficient. Still, LEPC SI can provide useful information at low acquisition cost when finer structural imaging and/or shallower targets are of interest (e.g., basin imaging if one can use higher frequency). For the current imaging resolution, LEPC SI could even assist in enhanced geothermal-system exploration together with magnetotelluric investigations. It is of importance for enhanced geothermal-system explorations to estimate the deeply lying conductive feature and the possible fault system between the thermal source (e.g., Moho) and the target basement (up to 10 km). The success of the method depends on the illumination of the receiver array by the coda wavefield. In our case, the results show illumination directivity at the TE-array for the coda-waves part we use. The main advantage of the method is that it turns the passive recordings into reflection recordings, which is not possible without using SI. Note that active-source measurements in the frequency bandwidth we use in this study are not always available. In this case, LEPC SI might complement the low-frequency bandwidth and would be a useful alternative approach.

Conclusions

We presented seismic interferometry for P-wave coda from local earthquakes (LEPC SI) in order to obtain crustal-scale reflection imaging without active sources. We applied LEPC SI with a linear array in the Malargüe region, Argentina, where a part of the Neuquén basin exists underneath. We compared SI by crosscorrelation, crosscoherence, and MDD, each followed by standard seismic processing from exploration seismology. For the MDD method, we found the truncated SVD scheme gave a more stable solution of the matrix inversion than the one by damped least-squares. This MDD result provided us slightly better structural imaging at our scale of interest among all LEPC SI approaches we investigated. We also interpreted not only the deep thrust fault but also possible melting zones that are previously suggested by active-seismic (including exploration well) as well as magnetotelluric surveys. Depending on the frequency-bandwidth, the availability of the local earthquakes, and the spatial sampling of receivers, LEPC SI has a potential to reveal not only the crustal-scale structure but also lithospheric-scale or basin-scale structures.

Acknowledgements

The data used in this study are collected using Java version of Windows Extracted from Event Data (JWEED) of Incorporated Research Institutions for Seismology (IRIS, http://www.iris.edu/dms/nodes/dmc/). This research is supported by the Division for Earth and Life Sciences (ALW) with financial aid from the Netherlands Organization for Scientific Research (NWO) with grant VIDI 864.11.009. The research of K.W. was supported by the Netherlands Research Centre for Integrated Solid Earth Sciences (ISES). The authors thank IRIS-PASSCAL for providing the seismic equipment and the Argentine Ministry of Science, Technology and Production Innovation for the financial support connected to the transportation of the equipment. The authors also thank Pierre Auger Observatory and the department of Civil Defense of Malargüe for the help during the data acquisition. The authors are thankful to Carlos Almagro Vidal, Max Holicki, Joost van der Neut, Iris Hartstra and Rémi Charton at Delft University of Technology and Issei Doi at Kyoto University for discussion. The authors are also grateful Nori Nakata, the associate editor, and four anonymous reviewers for their constructive comments that helped improve the quality of this manuscript. Seismic Analysis Code (SAC2000) was used for a part of the data processing. The maps were drawn with GenericMappingTool (GMT) (Wessel and Smith, 1991) and MATLAB.

Appendix A

Approximated Multidimensional Deconvolution (MDD)

Here, we show the derivation to obtain the approximate expression for seismic interferometry (SI) by MDD - equation (5) in the main text. First, we define the following relation in the frequency domain ω:

$$\bar{v}_z(\mathbf{x}_B,\omega) = \bar{v}_z^d(\mathbf{x}_B,\omega) + \bar{v}_z^c(\mathbf{x}_B,\omega), \tag{1}$$

where $\bar{v}_z(\mathbf{x}_B,\omega)$ is the vertical component (z) of the particle velocity vector in the absence of a free surface at the receiver $\mathbf{x}_B$ for a local earthquake in the subsurface, $\bar{v}_z^d(\mathbf{x}_B,\omega)$ represents only the direct arrival, and $\bar{v}_z^c(\mathbf{x}_B,\omega)$ represents the coda i.e., the scattering between inhomogeneities inside the medium. For the situation where there is a free surface at the receiver level, we also define the following relation:

$$v_z(\mathbf{x}_B,\omega) = v_z^d(\mathbf{x}_B,\omega) + v_z^c(\mathbf{x}_B,\omega), \tag{2}$$

which is the free-surface counterpart of equation (A-1). Note that $v_z^c(\mathbf{x}_B,\omega)$ is the coda wavefield we actually observe (see the light blue shades in Figure 6). Taking into account the fact that $v_z^d(\mathbf{x}_B,\omega) = 2\bar{v}_z^d(\mathbf{x}_B,\omega)$, equation (A-2) can be rewritten as

$$v_z(\mathbf{x}_B,\omega) = 2\bar{v}_z^d(\mathbf{x}_B,\omega) + v_z^c(\mathbf{x}_B,\omega). \tag{3}$$

Using equations (A-1) and (A-3), we can write for the scattered field

$$v_z^{scatt}(\mathbf{x}_B,\omega) = v_z(\mathbf{x}_B,\omega) - 2\bar{v}_z(\mathbf{x}_B,\omega) = v_z^c(\mathbf{x}_B,\omega) - 2\bar{v}_z^c(\mathbf{x}_B,\omega). \tag{4}$$

Here, we recall equation (63) in Wapenaar et al. (2011):

$$v_z^{scatt}(\mathbf{x}_B,\omega) = A \iint\limits_{\partial D_0} G_{z,z}^{scatt}(\mathbf{x}_B,\mathbf{x},\omega)\bar{v}_z(\mathbf{x},\omega)d^2\mathbf{x}, \tag{5}$$

where $G_{z,z}^{scatt}$ is the scattered Green's function and A is an amplitude-scaling factor due to the approximation that $\bar{v}_z(\mathbf{x},\omega)$ under the integral is proportional to the pressure measurement. The integral in equation (A-5) is taken along the receiver positions (Earth's surface ∂D_0). Substituting equations (A-1) and (A-4) into equation (A-5), we get

$$v_z^c(\mathbf{x}_B,\omega) - 2\bar{v}_z^c(\mathbf{x}_B,\omega) = A \iint\limits_{\partial D_0} G_{z,z}^{scatt}(\mathbf{x}_B,\mathbf{x},\omega)\left\{\bar{v}_z^d(\mathbf{x},\omega) + \bar{v}_z^c(\mathbf{x},\omega)\right\} d^2\mathbf{x}. \tag{6}$$

Multiplying equation (A-6) with $\bar{v}_z^c(\mathbf{x}_A,\omega)^*$ and summation over the available sources, we get

$$\begin{aligned}&\sum_{S=1}^{n}\left[v_z^c(\mathbf{x}_B,\omega)\left\{\bar{v}_z^c(\mathbf{x}_A,\omega)\right\}^*\right] - 2\Gamma(\mathbf{x}_B,\mathbf{x}_A,\omega) = \\ &A \iint\limits_{\partial D_0} G_{z,z}^{scatt,d}(\mathbf{x}_B,\mathbf{x},\omega)\left[\sum_{S=1}^{n}\left[\bar{v}_z^d(\mathbf{x},\omega)\left\{\bar{v}_z^c(\mathbf{x}_A,\omega)\right\}^*\right] + \Gamma(\mathbf{x},\mathbf{x}_A,\omega)\right] d^2\mathbf{x},\end{aligned} \tag{7}$$

where $*$ denotes the complex conjugate and Γ is the point-spread function (PSF, Wapenaar et al., 2011) defined as

$$\Gamma(\mathbf{x}_B,\mathbf{x}_A,\omega) = \sum_{S=1}^{n} \left[\bar{v}_z^c(\mathbf{x}_B,\omega)\left\{\bar{v}_z^c(\mathbf{x}_A,\omega)\right\}^*\right]. \tag{8}$$

Equation (A-7) can be also written as

$$\sum_{S=1}^{n} \left[v_z^c(\mathbf{x}_B,\omega)\left\{v_z^c(\mathbf{x}_A,\omega)\right\}^*\right] - 2\Gamma(\mathbf{x}_B,\mathbf{x}_A,\omega) + \sum_{S=1}^{n} \left[v_z^c(\mathbf{x}_B,\omega)\left[\left\{\bar{v}_z^c(\mathbf{x}_A,\omega) - v_z^c(\mathbf{x}_A,\omega)\right\}^*\right]\right] - \tag{9}$$

$$A\iint_{\partial D_0} G_{z,z}^{scatt,d}(\mathbf{x}_B,\mathbf{x},\omega)\sum_{S=1}^{n}\left[\bar{v}_z^d(\mathbf{x},\omega)\left\{\bar{v}_z^c(\mathbf{x}_A,\omega)\right\}^*\right]d^2\mathbf{x} = A\iint_{\partial D_0} G_{z,z}^{scatt,d}(\mathbf{x}_B,\mathbf{x},\omega)\Gamma(\mathbf{x},\mathbf{x}_A,\omega)d^2\mathbf{x}.$$

The third and fourth terms in the left-hand side of equation (A-9) retrieve events that are already retrieved by the first term in the left-hand side. Thus, the third and fourth terms can be seen as amplitude corrections to the events retrieved by the first term. If we neglect them to obtain equation (5), we will not obtain correct amplitudes in the left-hand side of equation (A-9) and we will introduce artifacts. Still, the MDD of the first two terms in the left-hand side by Γ will result in the compensation of the result retrieved from SI by crosscorrelation for inhomogeneous illumination. Furthermore, as Γ cannot be obtained directly, we approximate it by only the dominant arrivals in the result from SI by crosscorrelation (see for examples Figures 9c and 9f).

Appendix B

Truncated Singular-Value Decomposition (SVD)

In Figure B1, we show the truncated singular values for the TN- and TE-array.

References

Abe, S., E. Kurashimo, H. Sato, N. Hirata, T. Iwasaki, and T. Kawanaka, 2007, Interferometric seismic imaging of crustal structure using scattered teleseismic waves: Geophysical Research Letters, 34, L 19305, doi: 10.1029/2007GL030633.

Abercrombie, R., 2012, Comparison of direct and coda wave stress drop measurements for the Wells, Nevada, earthquake sequence: Journal of Geophysical Research, **118**, 1458-1470, doi: 10.1029/2012JB009638.

Aki, K., 1957, Space and time spectra of stationary waves with special reference to microtremors: Bulletin of the Earthquake Research Institute, University of Tokyo, **35**, 415–456.

Aki, K., A. Christoffersson, and E. S. Husebye, 1977, Determination of the three-dimensional seismic structure of the lithosphere: Journal of Geophysical Research, **82**, 456 277-296, doi: 10.1029/JB082i002p00277.

Almagro Vidal, C., D. Draganov, J. van der Neut, G. Drijkoningen, and K. Wapennar, 2014, Retrieval of reflections from ambient noise using illumination diagnosis: Geophysical Journal International, **198**, 1572–1584, doi: 10.1093/gji/ggu164.

Atkinson, G. M., and D. M. Boore, 1987, On the m_N, M relation for eastern North American earthquakes: Seismological Research Letters, **58**, 119-124, doi: 10.1785/gssrl.58.4.119.

Baltay, A., G. Prieto, and G. C. Beroza, 2010, Radiated seismic energy from coda measurements and no scaling in apparent stress with seismic moment: Journal of Geophysical Research, **115**, B08314, doi: 10.1029/2009JB006736.

Becker, J. J., D. T. Sandwell, W. H. F. Smith, J. Braud, B. Binder, J. Depner, D. Fabre, J. Factor, S. Ingalls, S. H. Kim, R. Ladner,K. Marks, S.

Nelson, A. Pharaoh, R. Trimmer, J. Von Rosenberg, G. Wallace, and P. Weatherall, 2009, Global bathymetry and elevation data at 30 arc seconds resolution: SRTM30_PLUS: Marine Geodesy, **32**, 355–371, doi: 10.1080/01490410903297766.

Borko, H., and M. D. Bernick, 1963, Automatic document classification: Journal of the Association for Computing Machinery, 10, 151-162, doi: 10.1145/321160.321165.

Boullenger, B., J. Hunziker, and D. Draganov, 2015, Reflection-response retrieval with seismic interferometry by multidimensional deconvolution from surface reflection data: 77th Conference and Exhibition, Extended abstracts, EAGE, We N112 06, doi: 10.3997/2214-4609.201412981.

Burd, A. I., J. R. Booker, R. Mackie, A. Favetto, and M. C. Pomposiello, 2014, Three-dimensional electrical conductivity in the mantle beneath the Payún Matrú Volcanic Field in the Andean backarc of Argentina near 36.5°S: evidence for decapitation of a mantle plume by resurgent upper mantle shear during slab steepening: Geophysical Journal International, **198**, 812–827, doi: 10.1093/gji/ggu145.

Calvert, A. J., L. A. Preston, and A. M. Farahbod, 2011, Sedimentary underplating at the Cascadia mantle-wedge corner revealed by seismic imaging: Nature Geoscience, **4**, 545-548, doi: 10.1038/NGEO1195.

Calvert, A. J., and S. E. McGeary, 2013, Seismic refl ection imaging of ultradeep roots beneath the eastern Aleutian island arc: Geology, **41,** 203-206, doi: 10.1130/G33683.1.

Campillo, M., and A. Paul, 2003, Long-range correlations in the diffuse seismic coda: Science, **299**, 547–549, doi: 10.1126/science.1078551.

Claerbout, J., 1968, Synthesis of a layered medium from its acoustic transmission response: Geophysics, **33**, 264-269, doi: 10.1190/1.1439927.

DeCelles, P. G., and K. A. Giles, 1996, Foreland basin systems: Basin Research, 8, 105-123, doi: 10.1046/j.1365-2117.1996.01491.x.

Doi, I., and H. Kawakata, 2013, High resolution spatial distribution of the velocity discontinuities in and around the swarm region beneath the Wakayama district, southwest Japan: Bulletin of the Seismological Society of America, **103**, 2135–2141, doi: 10.1785/0120120316.

Draganov, D., X. Campman, J. Thorbecke, A. Verdel, and K. Wapenaar, 2009, Reflection images from ambient seismic noise: Geophysics, **74**, A63-A67, doi: 10.1190/1.3193529.

Duvall Jr, T. L., S. M. Jefferies, J. W. Harvey, and M. A. Pomerantz, 1993, Time-distance helioseismology: Nature, **362**, 430-432, doi: 10.1038/362430a0.

Emoto, K., M. Campillo, F. Brenguier, X. Briand, and T. Takeda, 2015, Asymmetry of coda cross-correlation function: dependence of the epicentre location: Geophysical Journal International, **201**, 1313–1323, doi: 10.1093/gji/ggv081.

Farías, M., D. Comte, R. Charrier, J. Martinod, C. David, A. Tassara, and A. Fock, 2010, Crustal-scale structural architecture in central Chile based on seismicity and surface geology: implications for Andean mountain building: Tectonics, **29**, TC3006, doi: 10.1029/2009TC002480.

Garcia, D., 2010, Robust smoothing of gridded data in one and higher dimensions with missing values: Computational Statistics and Data Analysis, **54**, 1167-1178, doi: 10.1016/j.csda.2009.09.020.

Giambiagi, L., M. Ghiglione, E. Cristallini, and G. Bottesi, 2009, Kinematic models of basement/cover interaction: insights from the Malargüe fold and thrust belt, Mendoza, Argentina: Journal of Structural Geology, **31**, 1443-1457, doi: 10.1016/j.jsg.2009.10.006.

Giambiagi, L., J. Mescua, F. Bechis, A. Tassara, and G. Hoke, 2012, Thrust belts of the southern Central Andes: along-strike variations in shortening, topography, crustal geometry, and denudation: Geological Society of America Bulletin, **124**, 1339-1351, doi: 10.1130/B30609.1.

Gilbert, H., S. Beck, and G. Zandt, 2006, Lithospheric and upper mantle structure of central Chile and Argentina: Geophysical Journal International, **165**, 383–398, doi: 10.1111/j.1365-246X.2006.02867.x.

Granath, J. W., R. C. Whittaker, V. Singh, D. E. Bird, and M. G. Dinkelman, 2010, Full crustal seismic imaging in northeast Greenland: First Break, **28**, 79-83.

Golub, G. H., and C. F. van Loan, 1983, Matrix computations: The Johns Hopkins University Press.

Kanamori, H., and E. E. Brodsky, 2004, The physics of earthquakes: Reports on Progress in Physics, **67**, 1429-1496, doi: 10.1088/0034-4885/67/8/R03.

Kayal, J. R., 2008, Microearthquake seismology and seismotectonics of south Asia: Springer.

Kennett, B. L. N., E. R. Engdahl, and R. Buland, 1995, Constraints on seismic velocities in the earth from travel times: Geophysical Journal International, **122**, 108–124, doi: 10.1111/j.1365-246X.1995.tb03540.x.

Klema, V., and A. Laub, 1980, The singular value decomposition: its computation and some applications: IEEE Transactions on Automatic Control, **25**, 164–176, doi: 10.1109/TAC.1980.1102314.

Kraemer, P., J. Silvestro, F. Achilli, and W. Brinkworth, 2011, Kinematics of a hybrid thick-thin-skinned fold and thrust belt recorded in Neogene syntectonic wedge-top basins, southern central Andes between 35°

and 36° S, Malargüe, Argentina, AAPG Memoir, **94**, 245–270, doi: 10.1306/13251340M943099.

Langston, C. A., 1979, Structure under Mount Rainier, Washington, inferred from teleseismic body waves: Journal of Geophysical Research, **84**, 4749-4762, doi: 10.1029/JB084iB09p04749.

Mayeda, K., L. Malagnini, and W. R. Walter, 2007, A new spectral ratio method using narrow band coda envelopes: evidence for non-self-similarity in the Hector Mine sequence: Geophysical Research Letters, **34**, L11303, doi: 10.1029/2007GL030041.

Menke, W., 1989, Geophysical data analysis: discrete inverse theory: Academic Press.

Mescua, J. F., L. B. Giambiagi, and V. A. Ramos, 2013, Late Cretaceous uplift in the Malargüe fold-and-thrust belt (35ºS), southern Central Andes of Argentina and Chile: Andean Geology, **40**, 102-116, doi: 10.5027/andgeoV40n1-a05.

Minato, S., T. Matsuoka, T. Tsuji, D. Draganov, J. Hunziker, and K. Wapenaar, 2011, Seismic interferometry using multidimensional deconvolution and crosscorrelation for crosswell seismic reflection data without borehole sources: Geophysics, **76**, SA19-SA34, doi: 10.1190/1.3511357.

Minato, S., T. Matsuoka, and T. Tsuji, 2013, Singular-value decomposition analysis of source illumination in seismic interferometry by multidimensional deconvolution: Geophysics, **78**, Q25-Q34, doi: 10.1190/GEO2012-0245.1.

Nakahara, H., and M. M. Haney, 2015, Point spread functions for earthquake source imaging: an interpretation based on seismic interferometry: Geophysical Journal International, **202**, 54–61, doi: 10.1093/gji/ggv109.

Nakata, N., R. Snieder, T. Tsuji, T., K. Larner, and T. Matsuoka, 2011, Shear wave imaging from traffic noise using seismic interferometry by cross-coherence: Geophysics, **76**, SA97-SA106, doi: 10.1190/GEO2010-0188.1.

Nakata, N., R. Snieder, and M. Behm, 2014, Body-wave interferometry using regional earthquakes with multidimensional deconvolution after wavefield decomposition at free surface: Geophysical Journal International, **199**, 1125–1137, doi: 10.1093/gji/ggu316.

Nishitsuji, Y., E. Ruigrok, M. Gomez, and D. Draganov, 2014, Global-phase H/V spectral ratio for delineating the basin in the Malargüe region, Argentina: Seismological Research Letters, **85**, 1004-1011, doi: 10.1785/0220140054.

Nishitsuji, Y., E. Ruigrok, M. Gomez, K. Wapenaar, and D. Draganov, 2016, Reflection imaging of aseismic zone of the Nazca slab by global-phase seismic interferometry: Interpretation, (accepted).

Operto, S., J. Virieux, J. -X. Dessa, and G. Pascal, 2006, Crustal seismic imaging from multifold ocean bottom seismometer data by frequency domain full waveform tomography: Application to the eastern Nankai trough: Journal of Geophysical Research, **111**, B09306, doi: 10.1029/2005JB003835.

Panea, I., D. Draganov, C. Almagro Vidal, and V. Mocanu, 2014, Retrieval of reflections from ambient noise recorded in the Mizil area, Romania: Geophysics, **79**, Q31-Q42, doi: 10.1190/GEO2013-0292.1.

Paul, A., M. Campillo, L. Margerin, and E. Larose, 2005, Empirical synthesis of time-asymmetrical Green functions from the correlation of coda waves: Journal of Geophysical Research, **110**, B08302, doi: 10.1029/2004JB003521.

Pearson, K., 1901, On lines and planes of closest fit to systems of points in space: Philosophical Magazine, **2**, 559-572, doi: 10.1080/14786440109462720.

Prieto, G. A., J. F. Lawrence, and G. C. Beroza, 2009, Anelastic earth structure from the coherency of the ambient seismic field: Journal of Geophysical Research, **114**, B07303, doi: 10.1029/2008JB006067.

Ruigrok, E., D. Draganov, M. Gomez, J. Ruzzante, D. Torres, I. Lopes Pumarega, N. Barbero, A. Ramires, A. R. Castano Ganan, K. van Wijk, and K. Wapenaar, 2012, Malargüe seismic array: design and deployment for the temporary array: The European Physical Journal Plus, **127**, 126, doi: 10.1140/epjp/i2012-12126-7.

Ryberg, T., 2011, Body wave observations from cross-correlations of ambient seismic noise: A case study from the Karoo, RSA: Geophysical Research Letters, **38**, L13311, doi: 10.1029/2011GL047665.

Shapiro, N. M., and M. Campillo, 2004, Emergence of broadband Rayleigh waves from correlations of the ambient seismic noise: Geophysical Research Letters, **31**,L07614-1–L07614-4, doi: 10.1029/2004GL019491.

Singh, S. C., A. J. Harding, G. M. Kent, M. C. Sinha, V. Combier, S. Bazin, C. H. Tong, J.W. Pye, P. J. Barton, R.W. Hobbs, R. S. White, and J. A. Orcutt, 2006, Seismic reflection images of the Moho underlying melt sills at the East Pacific Rise: Nature, **442**, 287-290, doi: 10.1038/nature04939.

Slob, E., D. Draganov, and K. Wapenaar, 2007, Interferometric electromagnetic Green's functions representations using propagation invariants: Geophysical Journal International, **169**, 60–80, doi: 10.1111/j.1365-246X.2006.03296.x.

Snieder, R., 2004, Extracting the Green's function from the correlation of coda waves: a derivation based on stationary phase: Physical Review E, **69**, 046610, doi: 10.1103/PhysRevE.69.046610.

Snieder, R., and E. Şafak, 2006, Extracting the building response using seismic interferometry: theory and application to the Millikan library in Pasadena, California: Bulletin of the Seismological Society of America, **96**, 586-598, doi: 10.1785/0120050109.

Snieder, R., K. Wapenaar, and K. Larner, 2006, Spurious multiples in seismic interferometry of primaries: Geophysics, **71**, SI111-SI124, doi: 10.1190/1.2211507.

van der Neut, J., E. Ruigrok, and K. Wapenaar, 2010, Retrieving the Earth's reflection response by multi-dimensional deconvolution of ambient noise: 72nd Conference and Exhibition, EAGE, Extended abstracts, P406, doi: 10.3997/2214-4609.201401259.

van der Neut, J., J. Thorbecke, K. Metha, E. Slob, and K. Wapenaar, 2011, Controlled-source interferometric redatuming by crosscorrelation and multidimensional deconvolution in elastic media: Geophysics, **76**, SA63-SA76, doi: 10.1190/1.3580633.

Vasconcelos, I., and R. Snieder, 2008a, Interferometry by deconvolution, part 1—theory for elastic waves and application to drill-bit seismic imaging: Geophysics, **73**, S129–S141, doi: 10.1190/1.2904554.

Vasconcelos, I., and R. Snieder, 2008b, Interferometry by deconvolution, part 2—theory for acoustic waves and numerical examples: Geophysics, **73**, S115–S128, doi: 10.1190/1.2904985.

Wapenaar, K., 2004, Retrieving the elastodynamic Green's function of an arbitrary inhomogeneous medium by cross correlation: Physical Review Letters, **93**, 254301, doi: 10.1103/PhysRevLett.93.254301.

Wapenaar, K., J. van der Neut, and E. Ruigrok, 2008, Passive seismic interferometry by multidimensional deconvolution: Geophysics, **73**, A51-A56, doi: 10.1190/1.2976118.

Wapenaar, K., J. van der Neut, E. Ruigrok, D. Draganov, J. Hunziker, J.,

E. Slob, J. Thorbecke, and R. Snieder, 2011, Seismic interferometry by crosscorrelation and by multidimensional deconvolution: a systematic comparison: Geophysical Journal International, **185**, 1335–1364, doi: 10.1111/j.1365-246X.2011.05007.x.

Wessel, P., and W. H. F. Smith, 1991, Free software helps map and display data: EOS Transactions AGU, **72**, 441-448, doi: 10.1029/90EO00319.

Yilmaz, Ö., 1987, Seismic data analysis: SEG.

Zhan, Z., S. Ni, D. V. Helmberger, and R. W. Clayton, 2010, Retrieval of Moho-reflected shear wave arrivals from ambient seismic noise: Geophysical Journal International, **182**, 408–420, doi: 10.1111/j.1365-246X.2010.04625.x.

Zhao, J., Z. Jin, W. D. Mooney, N. Okaya, S. Wang,X. Gao, L. Tang, S. Pei, H. Liu, and Q. Xu, 2013, Crustal structure of the central Qaidam basin imaged by seismic wide-angle reflection/refraction profiling: Tectonophysics, **584**, 174-190, doi: 10.1016/j.tecto.2012.09.005.

Figure Captions

Figure 1.:

Distribution map of the local earthquakes ($2^\circ \leq$ epicentral distance $\leq 6^\circ$) used in our study. The 115 circles and 210 stars show the locations of the earthquakes recorded by the TN- (the white triangles) and TE-array (black triangles) parts of the MalARRgue array; the earthquakes are color-scaled as a function of their focal depth. The volcano symbol indicates the location of the Peteroa volcano. The green outline indicates an approximated location of the Neuquén basin (derived from Mescua et al., 2013). The blue polygon indicates an approximated location of the lake Llancanelo. The magenta solid and blue dashed lines indicate the location at which active-source seismic and an magnetotelluric sections are obtained by Kraemer et al. (2011) and Burd et al. (2014), respectively, which are discussed in Results and Interpretation of this paper.

Figure 2.:

Distribution of the back azimuth of the local earthquakes recorded by the TN-array and TE-array.

Figure 3.:

A schematic illustration of equation (5).

Figure 4.:

Power spectral densities for a local earthquake with M_b 4.0. The power spectral densities are computed for the TE-array.

Figure 5.:

Used window length of the P-wave coda as a function of epicentral distance. The traveltime curves are drawn using the regional velocity model from Farías et al. (2010) for depths down to 110 km and the ak135 model (Kennett et al., 1995) for greater depths. Light gray rectangular indicates the used epicentral distance, while the dark gray area indicates the the window lengths to be extracted for an earthquake characterized by a source depth of 100 km.

Figure 6.:

An example recording of a local earthquake on the vertical (left panel) and transverse component (right panel) of the stations from the TN-array. The areas highlighted in orange indicate the direct P-wave arrival from the local earthquake, while the green lines indicates the S-wave onset. The area highlighted in light blue indicates the P-wave coda to be extracted.

Figure 7.:

Number of original and interpolated events for each of the TN- and TE-array stations.

Figure 8.:

Retrieved zero-offset trace at station TE07 of the TE-array obtained using (a) autocorrelation without amplitude normalization, (b) energy normalization before autocorrelation, (c) maximum-amplitude normalization before autocorrelation, (d) maximum-amplitude normalization followed by spectral whitening before autocorrelation, and (e) autocoherence.

Figure 9.:

Retrieved common-source gather for a virtual source at (a) station TN11 of the TN-array before flipping, (b) after flipping the negative times, (d) station TE07 of the TE-array before flipping, (e) after flipping the negative times. The PSFs of (c) and (f) are extracted from the gray shaded areas in figures (a) and (d), respectively. The results are retrieved using correlation and after summation over the used local earthquakes.

Figure 10.:

Retrieved zero-offset traces using all events from (a) the TN-array (c) the TE-array. (b) and (d) are estimated source time functions from the zero-offset traces in (a) and (c), respectively, after application of time windowing.

Figure 11.:

A comparison of common-source gather: for station TN11 of the TN-array (a) before spiking deconvolution and muting the first breaks and (b) after spiking deconvolution and muting the first breaks and above; for station TE07 of the TE-array (c) before spiking deconvolution and muting the first breaks and (d) after spiking deconvolution and muting the first breaks and above.

Figure 12.:

Examples of velocity semblance of common midpoint gather for station TN11 of the TN-array (left panels) and station TE07 of the TE-array (right panels) with the regional velocity model of Farías et al. (2010) denoted by the magenta dashed lines.

Figure 13.:

A comparison of LEPC SI results for the TN-array using different SI theories: (a) cross-correlation after basement deconvolution without KTM; (b) same as (a) but with KTM; (c) same as (b) but for crosscoherence; (d) same as (b) but for MDD using the truncated SVD scheme.

Figure 14.:

Same as Figure 13 but for the TE-array.

Figure 15.:

Obtained MDD results using the damped least-square and the truncated SVD scheme in the f-x domain for virtual shots at: (a) station TN11; (b) station TE07 in comparison with the crosscorrelation (Figures 9a and 9d) and the PSF (Figures 9c and 9f).

Figure 16.:

Summarized interpretation on the crustal-scale reflection images beneath the TN-array obtained from: (a) LEPC SI (1-5 Hz) with the truncated MDD scheme; (b) global-phase SI (0.3-1 Hz) modified from Nishitsuji et al. (2016). The interpretation of the Moho and the magma chamber are after Gilbert et al. (2006) and Nishitsuji et al. (2016). The yellow dashed lines indicate our structural interpretation that can be traced for both the MDD and the global-phase SI results. The gray shades are the offset where the CMP folds are less than equal to 5. The cyan ellipses indicate the amplitude pockets that can be commonly interpretable between the MDD and the global-phase SI results.

Figure 17.:

Same as Figure 16, but for the TE-array. The blue ellipses indicate the dimming imaging parts that can be commonly interpretable between the MDD and the global-phase SI results. The green dashed line indicates our fault interpretation where the major deep thrust fault can be traced.

Figure B1.:

Truncated singular values for the TN- and TE-array. The white lines show where 10 % of the maximum singular value lie. We truncate the lower amplitude within the white line for MDD.

Table 1. Local earthquakes used in this study

Date (month/d/yr)	Time (hr:min:s)	Lat. (°N)	Lon. (°E)	Dep. (km)	M_b	Array ID
01/17/12	15:09:02	-30.814	-71.214	75	3.9	TE
01/17/12	23:21:34	-31.605	-71.686	31	5.5	TE
01/18/12	3:17:16	-31.589	-71.789	50	4.7	TE
01/18/12	11:33:03	-31.798	-68.397	10	4.6	TE
01/18/12	11:35:52	-31.665	-68.164	19	5.0	TE
01/19/12	3:58:17	-31.756	-68.657	15	4.6	TE
01/19/12	7:10:20	-31.635	-71.898	38	4.9	TE
01/19/12	8:22:49	-32.193	-71.213	87	3.9	TE
01/20/12	5:26:33	-31.273	-71.736	49	3.4	TE
01/20/12	6:05:41	-31.982	-68.843	117	3.5	TE
01/23/12	16:04:53	-36.455	-73.182	24	5.8	TE
01/23/12	16:29:30	-36.380	-73.267	25	4.0	TE
01/23/12	16:30:55	-36.457	-73.023	25	3.9	TE
01/23/12	17:22:06	-36.344	-73.443	4	5.0	TE
01/23/12	17:53:45	-36.472	-73.365	6	4.4	TE
01/23/12	21:55:15	-36.364	-73.304	28	5.0	TE
01/24/12	1:45:28	-34.525	-71.949	40	4.5	TE
01/24/12	16:08:48	-31.651	-67.078	150	3.7	TE
01/24/12	17:07:49	-31.760	-72.416	9	4.6	TE
01/26/12	2:23:10	-29.325	-68.081	118	3.6	TE
01/26/12	4:57:07	-34.831	-72.498	19	3.9	TE
01/27/12	2:24:10	-34.708	-71.824	17	4.1	TE
01/31/12	13:08:00	-33.817	-72.135	12	4.6	TE
01/31/12	19:40:03	-33.876	-71.997	18	4.0	TE
01/31/12	21:24:05	-32.788	-71.712	39	3.3	TE
02/01/12	2:43:19	-32.678	-71.336	52	4.8	TE
02/01/12	2:43:25	-32.950	-70.256	40	4.7	TE
02/01/12	2:43:27	-33.053	-70.851	44	4.7	TE
02/04/12	10:12:55	-38.551	-74.433	35	4.2	TE
02/05/12	3:42:08	-36.690	-73.243	38	4.7	TE
02/07/12	12:02:11	-37.902	-74.974	18	4.9	TE
02/10/12	2:05:22	-30.791	-71.304	57	4.9	TE
02/10/12	4:07:51	-30.735	-71.222	38	3.8	TE
02/11/12	2:58:17	-37.456	-73.884	20	5.6	TE
02/11/12	8:41:14	-36.851	-72.860	40	4.0	TE
02/14/12	5:58:02	-32.010	-70.034	103	4.5	TE
02/14/12	8:19:27	-34.948	-71.684	52	4.5	TE
02/15/12	7:36:14	-34.665	-72.958	10	4.4	TE
02/15/12	14:08:47	-35.209	-73.926	19	4.7	TE
02/16/12	22:01:46	-37.255	-74.245	5	4.2	TE
02/17/12	8:01:14	-37.208	-74.313	17	4.8	TE
02/17/12	8:01:19	-37.175	-73.646	14	4.8	TE
02/17/12	19:11:23	-37.233	-73.785	35	4.3	TE
02/18/12	2:06:27	-34.547	-72.098	29	4.5	TE
02/18/12	3:50:49	-37.104	-72.316	35	4.0	TE
02/18/12	17:44:48	-32.097	-71.771	18	4.9	TE
02/22/12	15:03:39	-33.089	-71.785	33	4.5	TE
02/22/12	22:38:40	-34.765	-71.809	47	4.0	TE
03/01/12	6:44:27	-38.331	-73.585	35	4.2	TE
03/01/12	18:41:47	-31.572	-69.273	96	4.6	TE
03/03/12	11:01:47	-30.348	-71.129	49	5.5	TE
03/03/12	22:12:55	-35.749	-72.800	13	4.9	TE
03/03/12	22:45:40	-35.731	-72.966	10	4.7	TE
03/03/12	23:41:30	-35.528	-72.726	28	4.6	TE
03/03/12	23:43:04	-35.740	-72.975	10	4.9	TE
03/09/12	0:43:36	-34.730	-72.781	39	4.3	TE
03/12/12	19:37:36	-34.969	-71.664	70	4.9	TE
03/16/12	6:20:12	-36.895	-73.596	27	4.7	TE
03/16/12	23:31:54	-33.606	-72.038	46	4.7	TE
03/17/12	1:36:00	-33.480	-72.372	21	4.0	TE
03/21/12	2:41:00	-35.789	-72.029	67	4.6	TE
03/23/12	9:25:32	-31.691	-69.025	95	4.3	TE
03/24/12	7:28:33	-33.052	-71.063	69	5.0	TE
03/25/12	22:37:06	-35.200	-72.217	41	6.5	TE
03/26/12	2:07:41	-34.994	-72.092	35	4.4	TE
03/27/12	2:46:12	-37.002	-73.275	23	4.5	TE
03/28/12	3:23:39	-35.541	-72.998	16	4.7	TE
03/30/12	7:12:52	-35.196	-72.187	38	4.5	TE/TN
03/31/12	21:52:56	-35.267	-72.089	43	4.4	TE/TN
04/01/12	19:09:57	-31.908	-71.322	65	4.9	TE/TN
04/03/12	2:11:03	-33.847	-72.757	32	5.0	TE/TN
04/06/12	1:30:12	-34.766	-71.608	37	3.7	TE
04/06/12	13:25:05	-38.226	-75.019	35	4.9	TN
04/06/12	17:11:27	-36.926	-73.899	10	4.7	TE
04/06/12	21:04:54	-35.598	-72.834	13	4.1	TE/TN
04/07/12	19:13:29	-37.408	-73.870	44	4.4	TE
04/13/12	6:13:16	-35.210	-72.020	40	4.7	TE/TN
04/15/12	18:58:21	-32.385	-71.940	27	4.4	TE/TN
04/16/12	10:34:14	-36.241	-73.352	27	4.3	TE/TN
04/17/12	3:50:16	-32.625	-71.365	29	6.2	TE/TN
04/17/12	4:03:18	-32.553	-71.366	40	4.9	TE/TN
04/17/12	17:53:57	-33.998	-72.342	11	4.1	TE/TN
04/17/12	23:37:36	-32.617	-71.591	25	3.5	TE/TN
04/19/12	1:14:06	-30.868	-71.188	65	4.7	TE/TN
04/21/12	5:14:37	-36.354	-72.709	63	4.0	TE/TN
04/21/12	22:18:11	-38.224	-74.289	31	4.7	TE/TN
04/27/12	17:58:24	-35.121	-71.901	43	4.7	TE/TN
04/27/12	18:34:38	-34.722	-71.721	43	4.7	TE/TN
04/28/12	20:46:48	-32.653	-71.829	5	4.1	TE
04/30/12	7:39:46	-29.868	-71.460	37	5.6	TE/TN
05/01/12	2:43:34	-29.456	-70.770	57	4.6	TN
05/01/12	20:52:14	-30.813	-71.935	22	4.8	TE
05/05/12	23:06:53	-31.474	-69.173	110	4.3	TE/TN
05/10/12	17:11:52	-37.249	-73.914	10	4.4	TE/TN
05/11/12	19:41:21	-32.901	-71.878	13	4.3	TE/TN
05/12/12	5:27:36	-34.896	-71.864	44	4.0	TE/TN
05/12/12	18:15:09	-34.523	-73.269	15	4.7	TE/TN
05/13/12	12:42:50	-32.740	-71.799	12	4.8	TE/TN
05/16/12	9:02:01	-36.901	-70.623	144	4.3	TE
05/16/12	10:15:36	-35.528	-71.312	118	4.3	TE
05/17/12	2:34:14	-31.777	-69.530	97	4.4	TE/TN
05/17/12	6:50:54	-32.697	-71.816	29	4.6	TE/TN
05/18/12	10:33:12	-31.807	-68.348	60	4.4	TE/TN
05/20/12	3:32:00	-30.782	-71.353	48	3.8	TE

05/21/12	5:15:26	-31.263	-68.507	84	4.3	TE/TN
05/21/12	11:13:33	-30.994	-71.648	59	4.4	TE
05/22/12	6:22:01	-32.244	-71.691	31	4.3	TE/TN
05/24/12	19:18:55	-36.912	-70.467	150	5.1	TE

05/31/12	8:27:17	-34.225	-71.751	20	4.5	TE/TN
06/01/12	18:19:52	-31.718	-68.635	19	4.7	TE
06/02/12	21:36:12	-36.174	-73.725	56	4.1	TE
06/07/12	7:40:54	-31.643	-71.219	36	4.7	TE/TN
06/11/12	9:50:59	-37.072	-73.661	40	4.2	TE
06/15/12	5:43:13	-38.188	-74.702	22	4.7	TE/TN
06/18/12	7:46:23	-36.692	-75.280	30	4.2	TE/TN
06/18/12	8:29:04	-33.009	-68.496	23	5.3	TE/TN
06/21/12	9:24:22	-35.523	-72.223	28	4.5	TE/TN
06/23/12	6:39:32	-34.563	-71.919	47	4.2	TE/TN
06/23/12	18:14:21	-31.580	-71.856	42	4.7	TE
06/25/12	13:38:17	-37.970	-74.821	10	4.6	TE/TN
06/26/12	7:09:27	-35.473	-71.676	84	4.5	TE
06/26/12	17:01:37	-37.758	-74.820	35	4.6	TE/TN
06/27/12	13:06:34	-31.701	-67.692	41	4.5	TE
06/27/12	22:04:25	-32.676	-71.722	20	3.9	TE/TN
06/28/12	10:33:17	-36.085	-73.270	30	4.3	TN
06/28/12	11:49:11	-31.447	-66.754	116	4.6	TE/TN
07/04/12	8:33:05	-38.040	-73.288	33	4.7	TE/TN
07/04/12	22:57:16	-37.631	-74.077	21	4.6	TE/TN
07/05/12	5:53:00	-34.494	-72.638	39	3.9	TE/TN
07/07/12	10:52:15	-32.502	-71.600	33	4.8	TE/TN
07/09/12	1:44:27	-35.213	-72.069	50	4.5	TE/TN
07/09/12	12:56:37	-33.061	-68.263	142	4.6	TE/TN
07/09/12	14:24:37	-37.700	-73.870	30	4.3	TE/TN
07/15/12	8:23:25	-33.483	-67.477	200	4.6	TE/TN
07/17/12	22:03:26	-31.298	-71.210	52	4.0	TE
07/30/12	18:49:45	-35.771	-74.163	44	4.8	TE/TN
08/02/12	15:01:32	-31.862	-68.575	20	4.3	TE/TN
08/04/12	13:11:46	-32.835	-69.175	33	4.3	TE/TN
08/04/12	19:05:39	-31.928	-69.358	119	5.0	TE/TN
08/17/12	20:19:54	-35.613	-73.615	20	4.7	TE/TN
08/23/12	19:03:48	-35.776	-73.462	11	4.8	TE/TN
08/24/12	22:30:01	-33.434	-72.310	42	4.7	TE/TN
08/27/12	1:29:45	-31.386	-67.746	105	4.2	TE/TN
08/27/12	4:17:56	-34.709	-71.762	55	4.0	TE/TN
08/28/12	8:11:25	-32.418	-71.169	44	4.8	TE/TN
08/30/12	8:04:40	-37.199	-73.397	23	5.0	TE/TN
09/04/12	5:30:17	-32.516	-69.916	112	4.5	TE/TN
09/06/12	18:58:03	-36.719	-73.408	35	4.7	TE/TN
09/11/12	6:35:38	-31.875	-68.350	124	5.1	TE/TN
09/11/12	7:24:37	-38.001	-73.860	21	4.6	TE/TN
09/12/12	9:20:58	-32.606	-68.692	139	4.6	TE/TN
09/15/12	0:40:16	-34.638	-72.564	34	4.7	TE/TN
09/15/12	0:50:45	-34.622	-72.923	26	4.5	TE/TN
09/15/12	9:37:18	-32.853	-66.601	36	4.6	TE/TN
09/18/12	3:53:30	-31.893	-69.262	26	4.4	TE/TN
09/20/12	10:07:07	-34.436	-71.951	60	4.5	TE/TN
09/21/12	9:22:26	-32.947	-69.739	101	4.4	TE/TN
09/28/12	3:11:50	-31.430	-67.915	96	4.1	TE/TN
09/28/12	19:21:47	-34.603	-73.369	10	4.3	TE
10/01/12	8:06:29	-30.786	-71.184	56	4.6	TE/TN
10/05/12	8:44:51	-34.899	-71.937	60	4.4	TE/TN
10/06/12	3:18:15	-32.132	-72.107	9	4.6	TE
10/06/12	22:49:38	-32.127	-71.860	7	4.3	TE
10/08/12	13:03:42	-34.654	-73.639	14	4.2	TE/TN
10/09/12	3:30:33	-29.393	-69.211	97	4.8	TE/TN
10/10/12	18:05:02	-34.039	-71.675	33	4.1	TE/TN
10/11/12	2:38:30	-34.000	-72.500	32	4.6	TE/TN
10/11/12	4:38:24	-33.996	-72.442	35	4.7	TE/TN
10/11/12	17:22:10	-32.865	-70.310	82	5.5	TE/TN
10/11/12	21:36:08	-34.011	-72.483	43	4.2	TE/TN
10/14/12	3:37:30	-34.606	-72.209	15	4.5	TE/TN
10/14/12	10:50:17	-35.310	-73.932	21	4.8	TE/TN
10/15/12	21:04:21	-31.814	-71.787	24	5.2	TE
10/18/12	4:38:00	-31.827	-72.034	29	4.5	TE
10/18/12	5:23:14	-34.689	-71.906	43	4.2	TE/TN
10/19/12	5:35:22	-31.793	-72.024	43	3.8	TE
10/19/12	22:48:18	-31.758	-71.950	10	4.6	TE
10/20/12	0:25:48	-32.251	-72.141	22	4.4	TE/TN
10/21/12	11:40:36	-37.658	-73.723	15	4.5	TE/TN
10/24/12	3:46:30	-31.698	-72.069	44	4.7	TE
10/25/12	5:37:58	-32.773	-70.165	105	4.8	TE/TN
10/25/12	19:25:41	-29.568	-70.968	69	4.1	TE
10/27/12	12:33:05	-33.642	-72.006	47	4.4	TE/TN
10/28/12	1:43:00	-33.404	-71.608	34	3.9	TE/TN
11/01/12	23:43:38	-31.794	-67.119	109	4.3	TE/TN
11/02/12	23:42:36	-34.848	-71.789	60	4.5	TE/TN
11/04/12	14:33:06	-31.729	-71.885	43	4.2	TE/TN
11/07/12	15:16:27	-30.780	-71.934	34	4.6	TE
11/07/12	18:37:50	-37.948	-73.141	38	4.4	TE
11/07/12	22:41:33	-37.512	-72.985	39	4.8	TE/TN
11/08/12	6:24:10	-32.710	-71.310	46	4.3	TE/TN
11/08/12	23:57:57	-31.882	-69.070	107	4.6	TE
11/09/12	6:31:44	-33.427	-67.479	187	4.1	TE/TN
11/11/12	5:10:56	-33.962	-72.132	13	4.6	TE/TN
11/11/12	5:46:48	-33.977	-72.183	16	4.8	TE/TN
11/11/12	7:24:21	-33.973	-72.272	38	4.4	TE/TN
11/15/12	20:32:37	-32.666	-71.825	23	4.7	TE
11/15/12	23:41:02	-30.988	-71.171	66	4.2	TE
11/17/12	23:51:39	-37.594	-73.825	21	4.0	TE
11/18/12	13:29:28	-38.286	-73.690	56	4.7	TE/TN
11/19/12	14:08:59	-33.969	-72.150	1	4.2	TE/TN
11/19/12	16:45:50	-33.928	-72.170	11	5.1	TE/TN
11/20/12	16:23:25	-33.921	-72.254	16	5.4	TE/TN
11/21/12	18:16:38	-33.931	-72.100	19	5.1	TE/TN
11/21/12	21:36:23	-33.939	-71.868	18	5.7	TE/TN
11/21/12	22:51:23	-34.012	-72.305	35	4.2	TE/TN
11/21/12	22:52:29	-33.916	-71.994	16	5.2	TE/TN
11/29/12	0:09:39	-32.910	-69.106	8	5.0	TE/TN
11/29/12	20:40:59	-36.426	-71.082	3	4.2	TE
12/02/12	3:29:23	-35.541	-72.766	15	4.3	TE/TN
12/04/12	9:26:14	-32.710	-71.751	38	4.6	TE/TN
12/10/12	15:25:47	-38.932	-72.862	33	4.8	TN
12/16/12	22:46:11	-33.803	-71.408	63	4.7	TE/TN
12/17/12	8:38:25	-32.342	-65.287	20	4.4	TN
12/18/12	0:45:03	-33.645	-71.187	66	3.7	TE/TN

Date, Time, Lat., Lon., Dep. and M_{W}, the moment magnitude, are provided by USGS (http://earthquake.usgs.gov/earthquakes/). For Array ID, TE and TN indicate TE-array and TN-array, respectively.

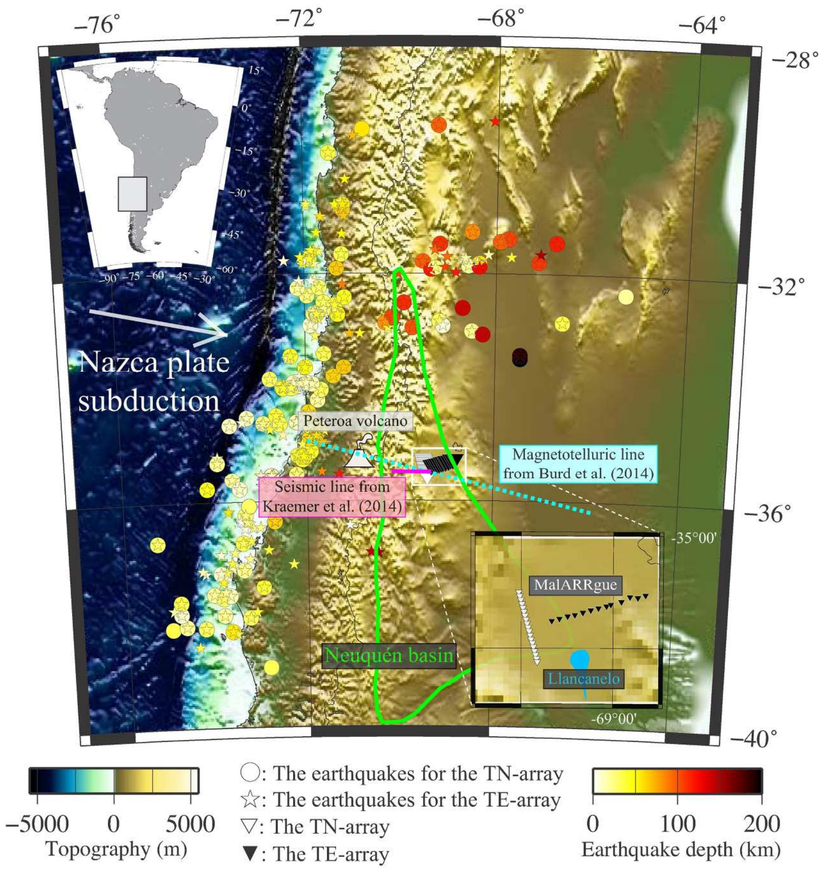

Figure 1.: Distribution map of the local earthquakes (2° ≤ epicentral distance ≤ 6°) used in our study. The 115 circles and 210 stars show the locations of the earthquakes recorded by the TN- (the white triangles) and TE-array (black triangles) parts of the MalARRgue array; the earthquakes are color-scaled as a function of their focal depth. The volcano symbol indicates the location of the Peteroa volcano. The green outline indicates an approximated location of the Neuquén basin (derived from Mescua et al., 2013). The blue polygon indicates an approximated location of the lake Llancanelo. The magenta solid and blue dashed lines indicate the location at which active-source seismic and an magnetotelluric sections are obtained by Kraemer et al. (2011) and Burd et al. (2014), respectively, which are discussed in Results and Interpretation of this paper.
225x259mm (300 x 300 DPI)

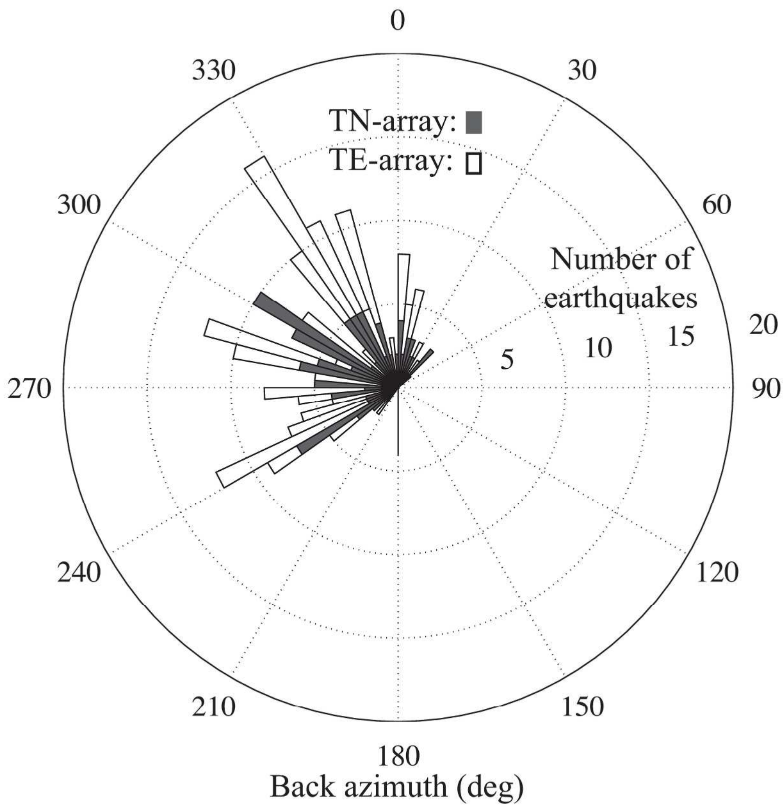

Figure 2.: Distribution of the back azimuth of the local earthquakes recorded by the TN-array and TE-array.
230x186mm (300 x 300 DPI)

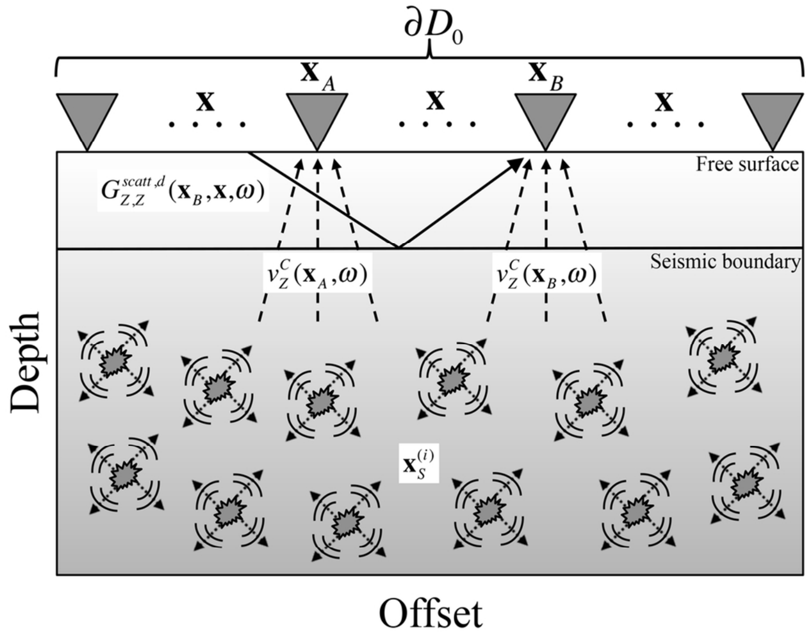

Figure 3.: A schematic illustration of equation (5).
108x88mm (300 x 300 DPI)

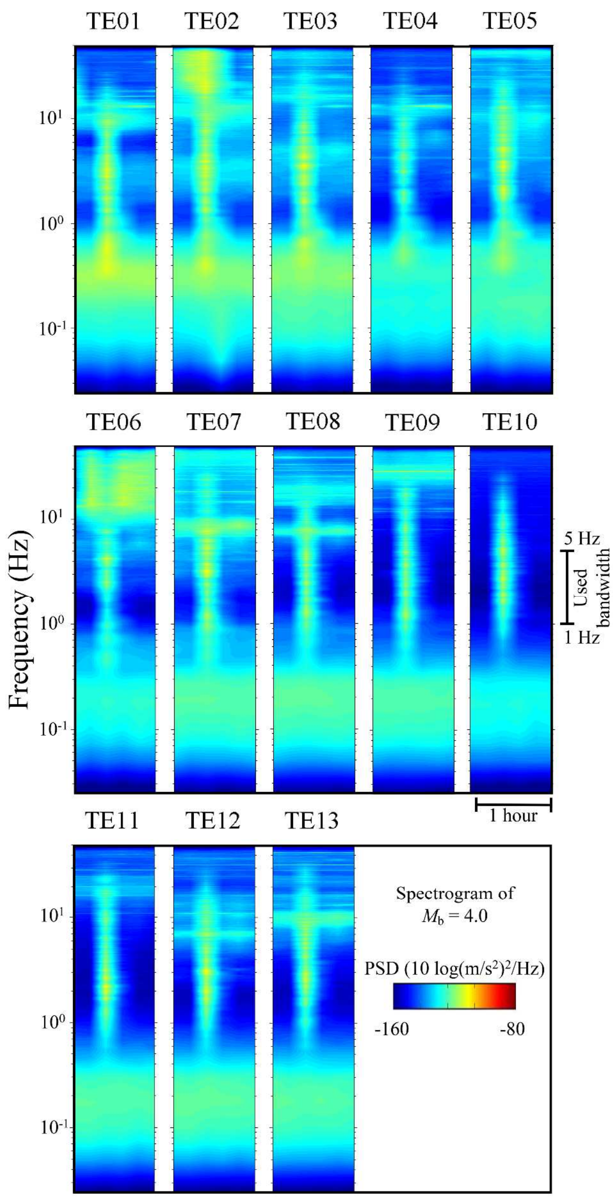

Figure 4.: Power spectral densities for a local earthquake with Mb 4.0. The power spectral densities are computed for the TE-array.
177x317mm (600 x 600 DPI)

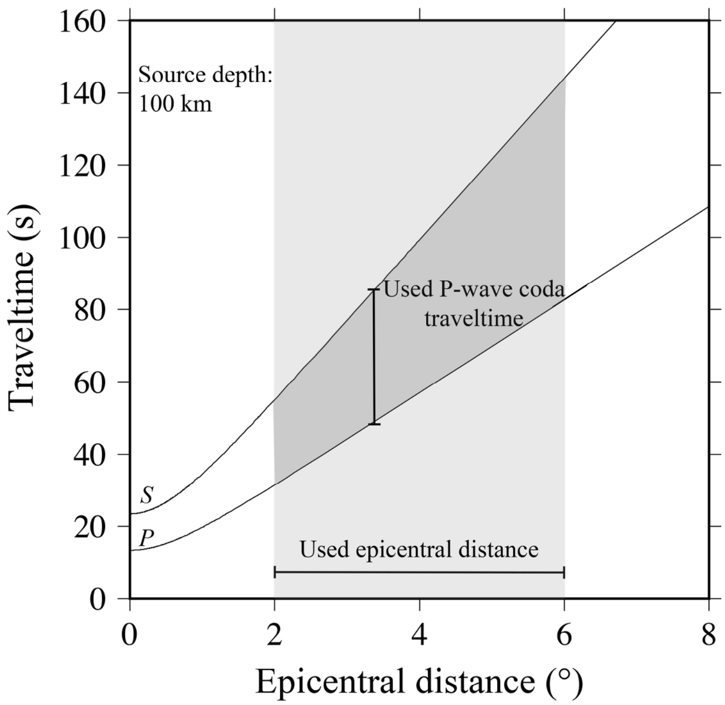

Figure 5.: Used window length of the P-wave coda as a function of epicentral distance. The traveltime curves are drawn using the regional velocity model from Farías et al. (2010) for depths down to 110 km and the ak135 model (Kennett et al., 1995) for greater depths. Light gray rectangular indicates the used epicentral distance, while the dark gray area indicates the the window lengths to be extracted for an earthquake characterized by a source depth of 100 km.
190x210mm (300 x 300 DPI)

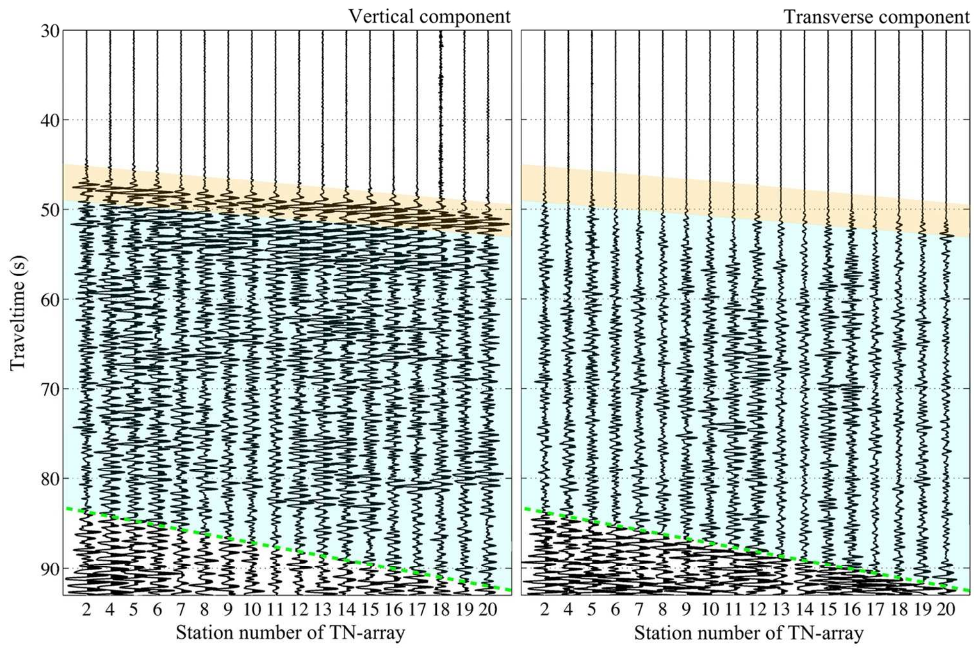

Figure 6.: An example recording of a local earthquake on the vertical (left panel) and transverse component (right panel) of the stations from the TN-array. The areas highlighted in orange indicate the direct P-wave arrival from the local earthquake, while the green lines indicates the S-wave onset. The area highlighted in light blue indicates the P-wave coda to be extracted.
130x88mm (300 x 300 DPI)

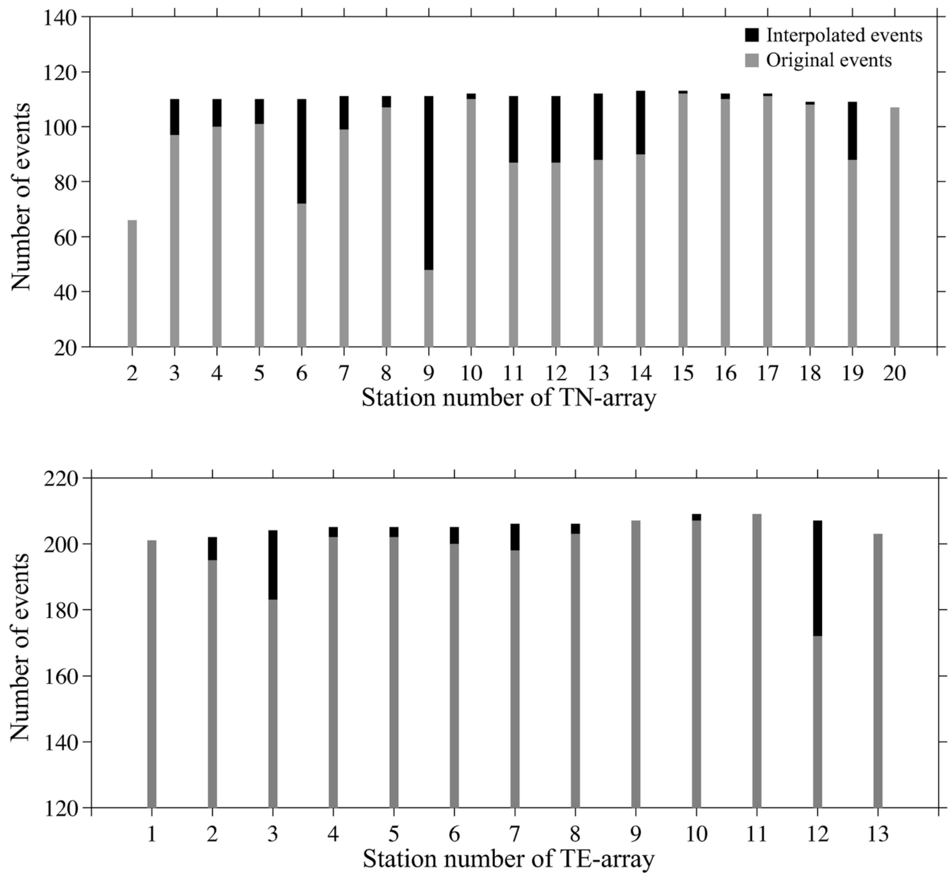

Figure 7.: Number of original and interpolated events for each of the TN- and TE-array stations.
152x138mm (300 x 300 DPI)

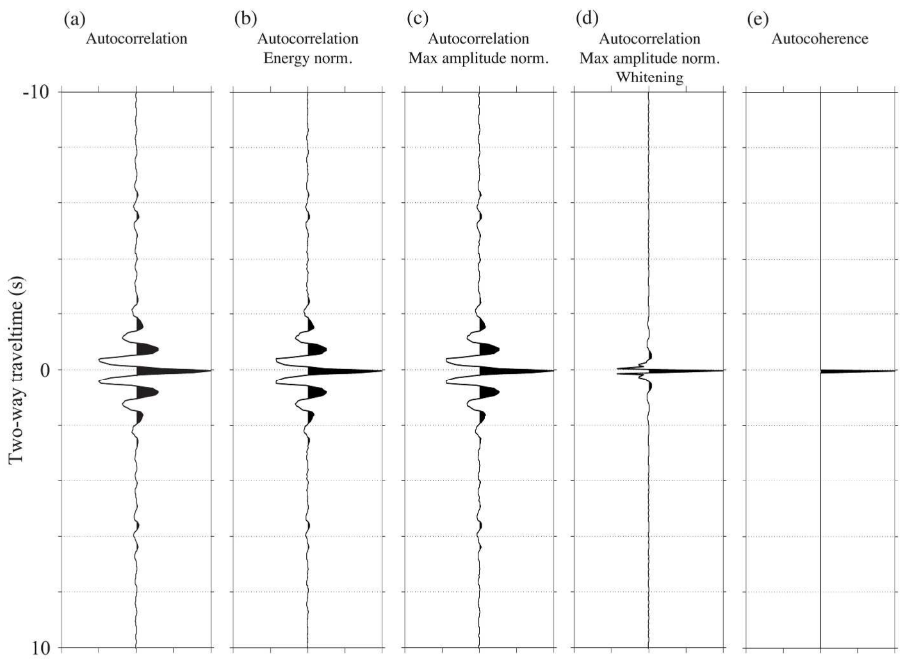

Figure 8.: Retrieved zero-offset trace at station TE07 of the TE-array obtained using (a) autocorrelation without amplitude normalization, (b) energy normalization before autocorrelation, (c) maximum-amplitude normalization before autocorrelation, (d) maximum-amplitude normalization followed by spectral whitening before autocorrelation, and (e) autocoherence.
247x174mm (300 x 300 DPI)

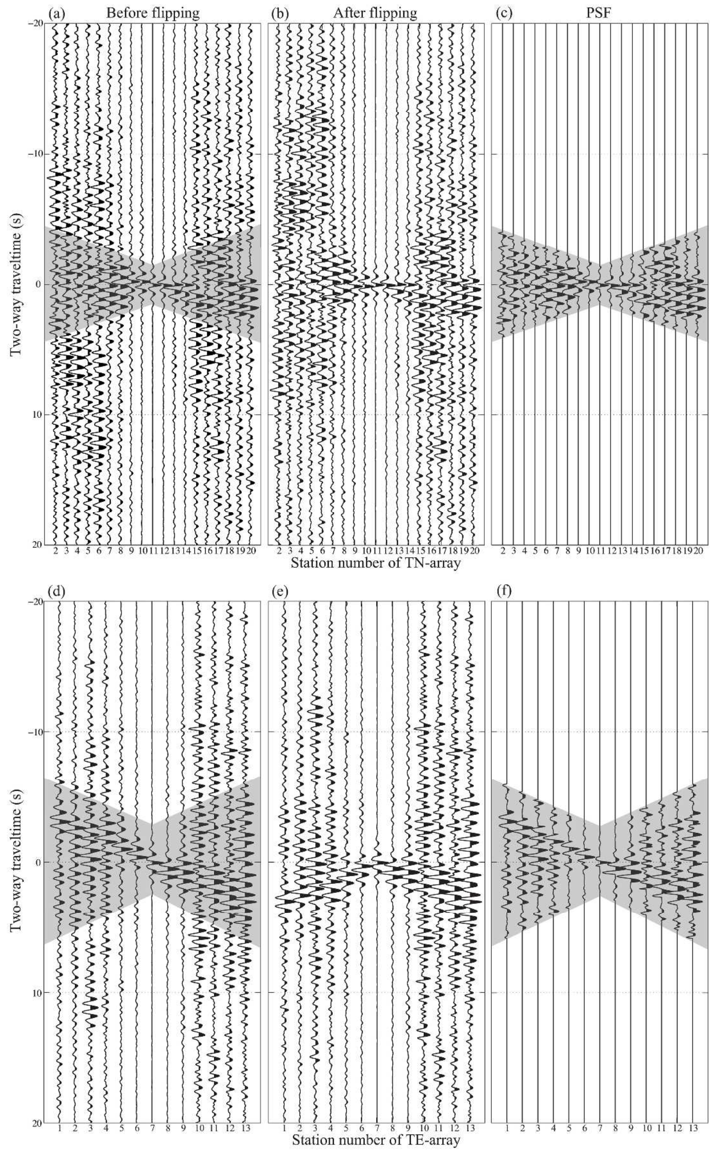

Figure 9.: Retrieved common-source gather for a virtual source at (a) station TN11 of the TN-array before flipping, (b) after flipping the negative times, (d) station TE07 of the TE-array before flipping, (e) after flipping the negative times. The PSFs of (c) and (f) are extracted from the gray shaded areas in figures (a) and (d), respectively. The results are retrieved using correlation and after summation over the used local earthquakes.
305x480mm (300 x 300 DPI)

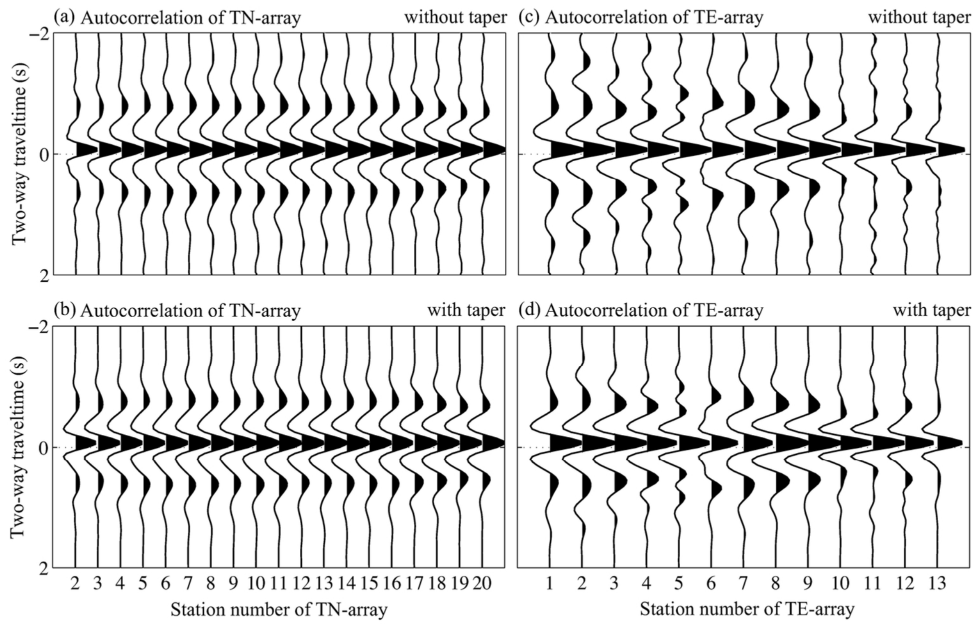

Figure 10.: Retrieved zero-offset traces using all events from (a) the TN-array (c) the TE-array. (b) and (d) are estimated source time functions from the zero-offset traces in (a) and (c), respectively, after application of time windowing.
133x86mm (300 x 300 DPI)

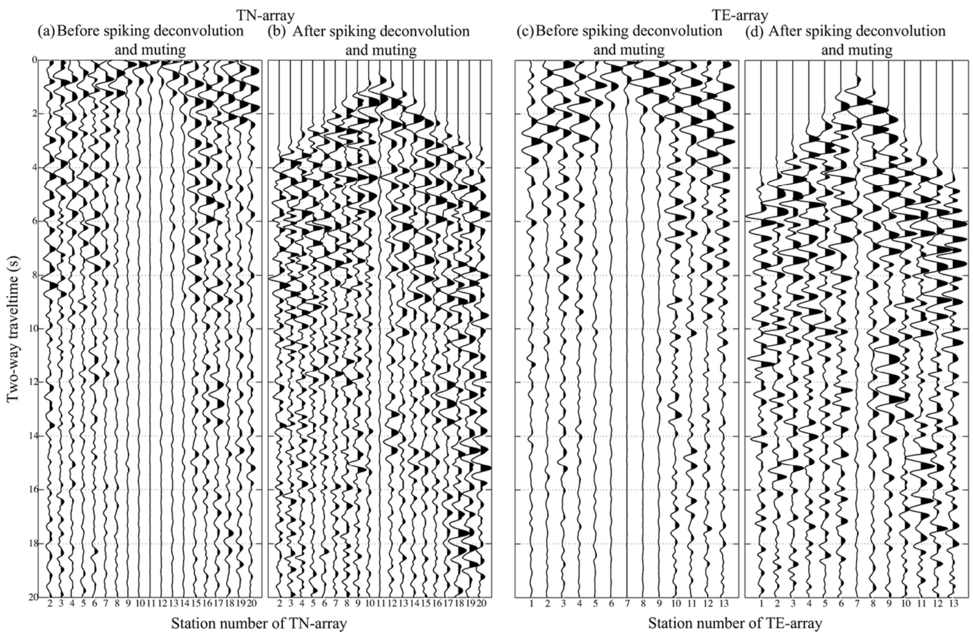

Figure 11.: A comparison of common-source gather: for station TN11 of the TN-array (a) before spiking deconvolution and muting the first breaks and (b) after spiking deconvolution and muting the first breaks and above; for station TE07 of the TE-array (c) before spiking deconvolution and muting the first breaks and (d) after spiking deconvolution and muting the first breaks and above.
129x84mm (300 x 300 DPI)

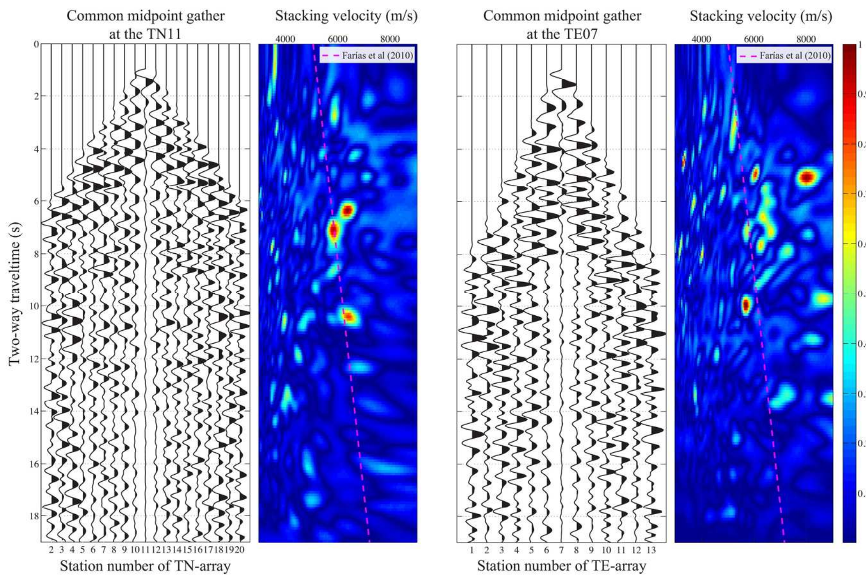

Figure 12.: Examples of velocity semblance of common midpoint gather for station TN11 of the TN-array (left panels) and station TE07 of the TE-array (right panels) with the regional velocity model of Farías et al. (2010) denoted by the magenta dashed lines.
190x142mm (300 x 300 DPI)

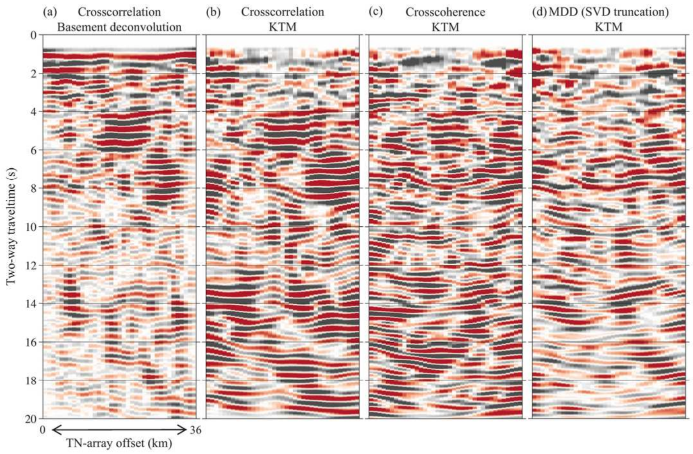

Figure 13.: A comparison of LEPC SI results for the TN-array using different SI theories: (a) crosscorrelation after basement deconvolution without KTM; (b) same as (a) but with KTM; (c) same as (b) but for crosscoherence; (d) same as (b) but for MDD using the truncated SVD scheme.
169x84mm (300 x 300 DPI)

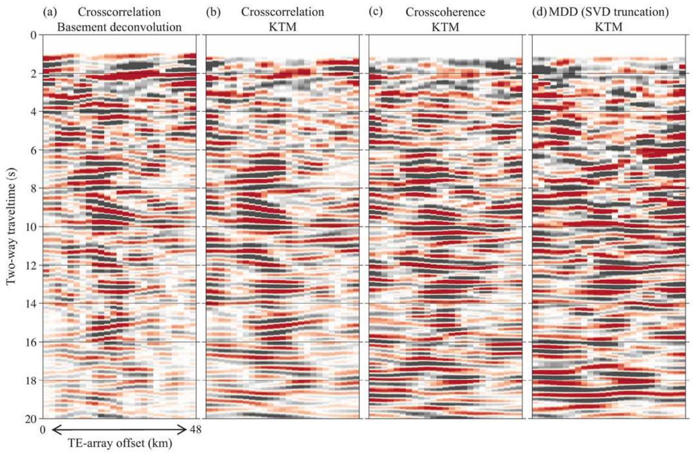

Figure 14.: Same as Figure 13 but for the TE-array.
169x84mm (300 x 300 DPI)

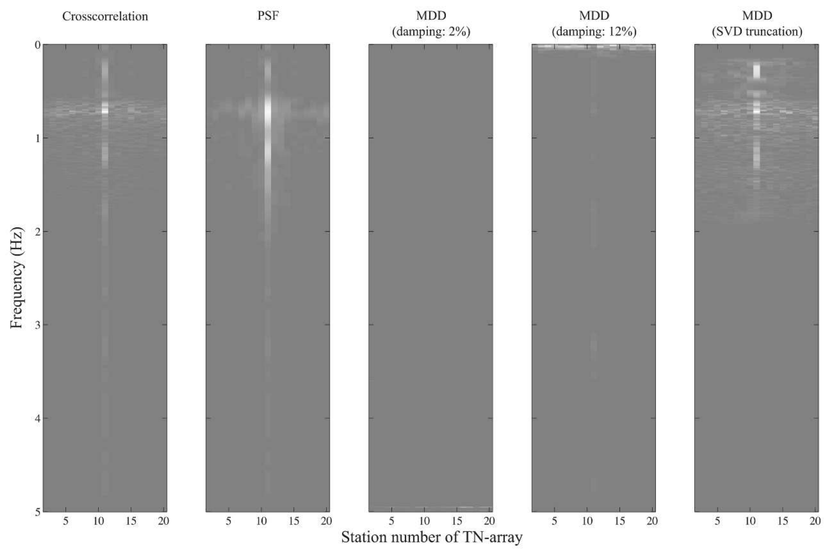

Figure 15.: Obtained MDD results using the damped least-square and the truncated SVD scheme in the f-x domain for virtual shots at: (a) station TN11; (b) station TE07 in comparison with the crosscorrelation (Figures 9a and 9d) and the PSF (Figures 9c and 9f).
249x143mm (300 x 300 DPI)

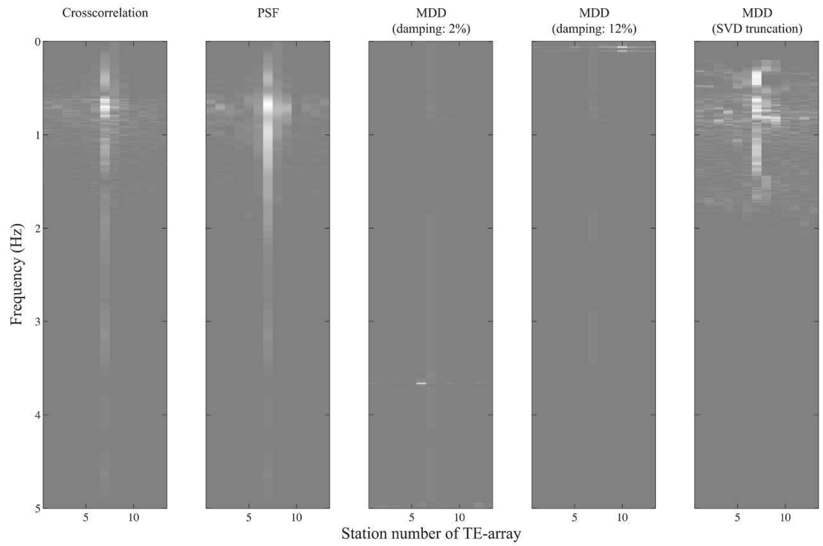

Figure 15.: Obtained MDD results using the damped least-square and the truncated SVD scheme in the f-x domain for virtual shots at: (a) station TN11; (b) station TE07 in comparison with the crosscorrelation (Figures 9a and 9d) and the PSF (Figures 9c and 9f).
249x143mm (300 x 300 DPI)

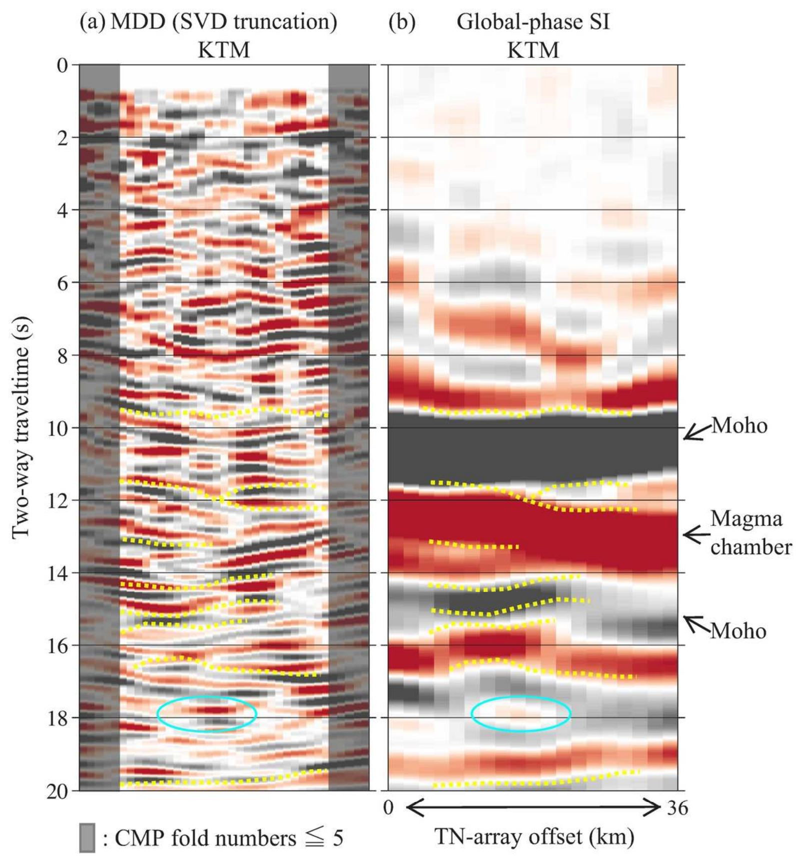

Figure 16.: Summarized interpretation on the crustal-scale reflection images beneath the TN-array obtained from: (a) LEPC SI (1-5 Hz) with the truncated MDD scheme; (b) global-phase SI (0.3-1 Hz) modified from Nishitsuji et al. (2016). The interpretation of the Moho and the magma chamber are after Gilbert et al. (2006) and Nishitsuji et al. (2016). The yellow dashed lines indicate our structural interpretation that can be traced for both the MDD and the global-phase SI results. The gray shades are the offset where the CMP folds are less than equal to 5. The cyan ellipses indicate the amplitude pockets that can be commonly interpretable between the MDD and the global-phase SI results.
167x158mm (300 x 300 DPI)

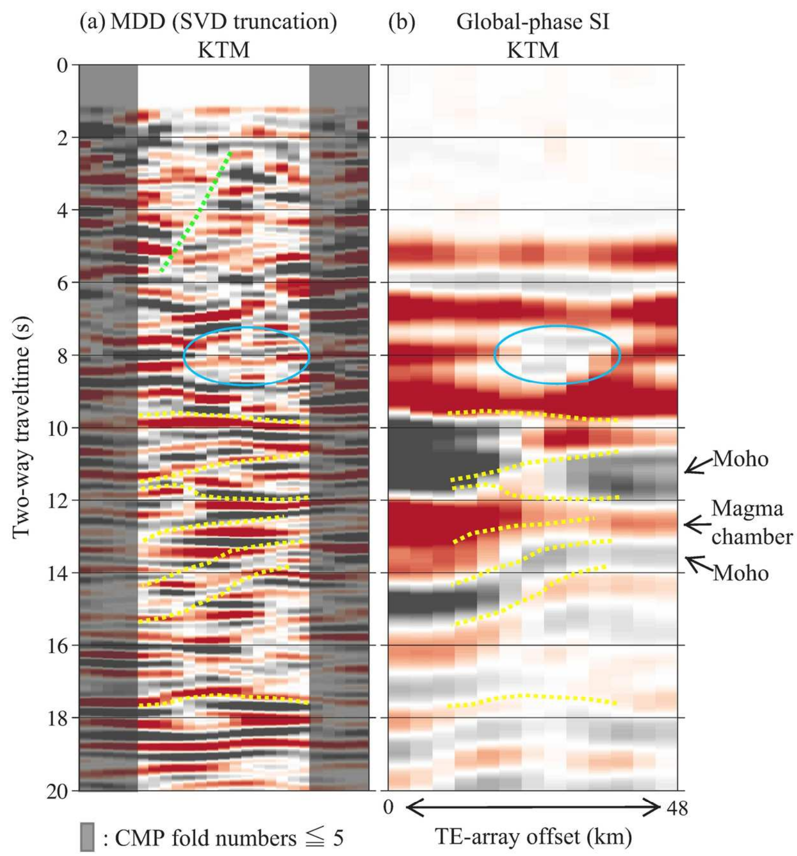

Figure 17.: Same as Figure 16, but for the TE-array. The blue ellipses indicate the dimming imaging parts that can be commonly interpretable between the MDD and the global-phase SI results. The green dashed line indicates our fault interpretation where the major deep thrust fault can be traced.
167x158mm (300 x 300 DPI)

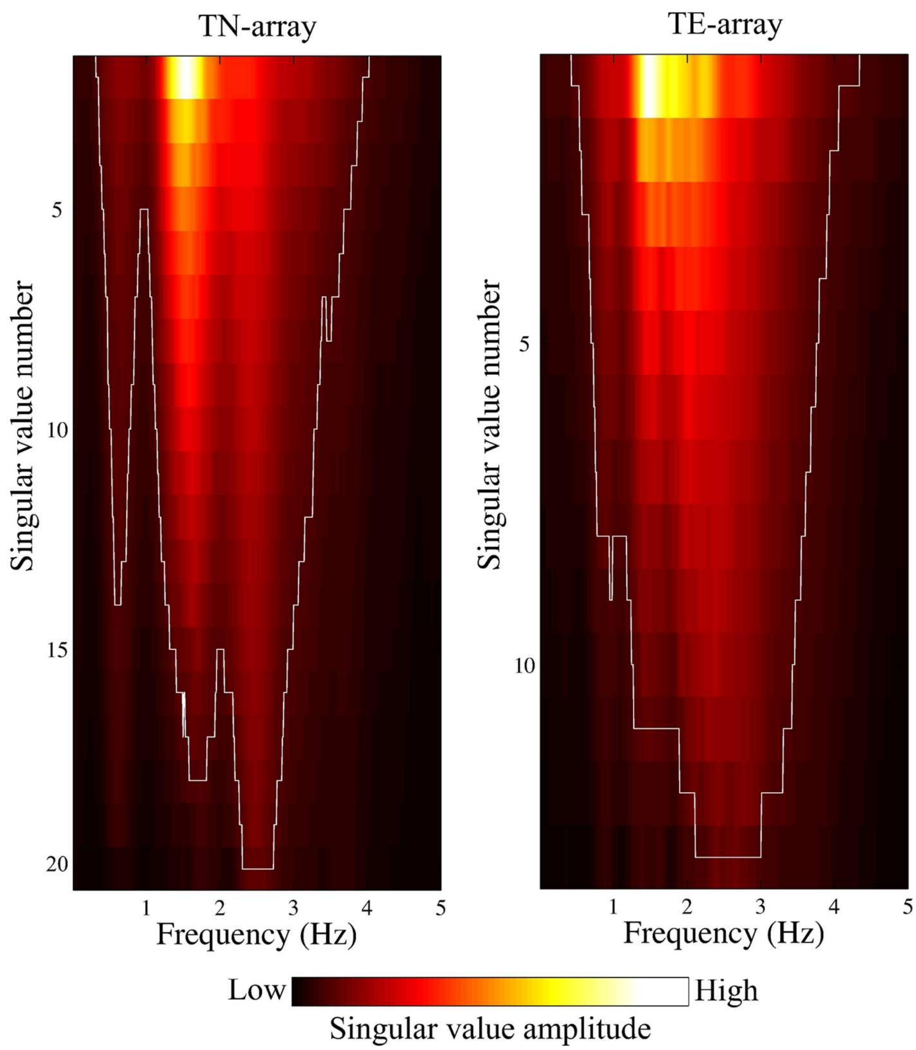

Figure B1.: Truncated singular values for the TN- and TE-array. The white lines show where 10 % of the maximum singular value lie. We truncate the lower amplitude within the white line for MDD.
141x156mm (300 x 300 DPI)